International Journal of Greenhouse Gas Control 118 (2022) 103685

Contents lists available at ScienceDirect

International Journal of Greenhouse Gas Control

journal homepage: www.elsevier.com/locate/ijggc

# Evaluation of MBTSA technology for $CO_2$ capture from waste-to-energy plants

Giorgia Mondino [*,a,b], Carlos A. Grande [b], Richard Blom [b], Lars O. Nord [a]

[a] NTNU - Norwegian University of Science and Technology, Department of Energy and Process Engineering, Trondheim, Norway
[b] SINTEF Industry, PO Box 124 Blindern, Oslo N0314, Norway

ARTICLE INFO

*Keywords:*
Carbon capture and storage (CCS)
TSA
Solid sorbent
Activated carbon
Process simulation
Waste incinerator
Heat transfer coefficient

ABSTRACT

Moving bed temperature swing adsorption (MBTSA) is a promising technology for $CO_2$ capture from flue gases. In a MBTSA unit, a selective adsorbent material is circulated between a low-temperature stage where it removes $CO_2$ from the flue gas and a higher-temperature zone where it desorbs $CO_2$ at higher purity. The main benefits of MBTSA are low pressure drops in the adsorption zone and the possibility to heat the adsorbent faster than standard adsorption technologies. This work evaluated via process simulations the use of the MBTSA technology for $CO_2$ capture from an industrial-scale waste-to-energy plant. To assess the technology with realistic parameters, we measured heat transfer coefficients in the heating section of a new MBTSA demonstrator unit using activated carbon spheres. The heating device was produced by 3D printing, and has rectangular channels on the gas-solid side rotated at 45° to facilitate solid flow. The heat transfer coefficients increased with the flow rate of activated carbon particles, and the highest value of 120 $W/m^2K$ was measured for a sorbent mass flux of 3.5 $kg/m^2s$. This information was used as input for the process simulations, and allowed a tailored and realistic design of an MBTSA unit capturing more than 90% of the exhaust $CO_2$ with a purity above 95%. The rather high specific heat duty of the process (5.7 MJ/kg $CO_2$) can be attributed to the low adsorption capacity of the activated carbon. In this respect, significant improvements can be expected by employing adsorbents with higher adsorption capacity and selectivity, such as zeolites or metal-organic frameworks.

## 1. Introduction

The production of municipal solid waste is expected to keep increasing as a result of the rapid grow of population and living standards around the world (Kaza et al., 2018). Waste-to-energy plants represent a key technology to manage the increasing quantities of solid waste, reduce the methane emissions associated with landfilled waste, and satisfy the rising energy demand (Brunner and Rechberger, 2015). In addition, the integration of waste-to-energy plants with Carbon Capture and Storage (CCS) technologies has the potential to make waste a net-zero or even negative emission energy source (Haaf et al., 2020; Kearns, 2019; Turan et al., 2021).

In the context of post-combustion $CO_2$ capture, adsorption-based processes are considered a promising alternative to the current benchmark technology based on amine solutions, which suffers from high energy consumption and environmental as well as corrosion issues related to solvent degradation (Bui et al., 2018; Sjostrom and Krutka, 2010). Adsorption-based processes make use of porous solids capable of: i) removing the $CO_2$ from the flue gas by selectively adsorbing it onto their surface and ii) releasing the adsorbed $CO_2$ when subjected to a change of pressure or temperature. The former property enables the separation of the $CO_2$ from the rest of the flue gas components, while the latter is responsible for the regeneration of the adsorbent, enabling a cyclic operation and permitting the recovery of $CO_2$ in a high purity stream. When the regeneration of the adsorbent is carried out by reducing the pressure of the system, the process is referred to as Pressure Swing Adsorption (PSA) or Vacuum Swing Adsorption (VSA), depending on the operating pressure, while the term Temperature Swing Adsorption (TSA) is used to indicate processes where the adsorbent is regenerated by an increase in temperature upon external heat supply. In large-scale post-combustion capture applications, like waste-to-energy

*Abbreviations:* CCS, Carbon Capture and Storage; CFDM, Centered Finite Difference Method; CHP, Combined Heat and Power; GHG, Greenhouse Gases; HTC, Heat Transfer Coefficient; HX, Heat Exchanger; LDF, Linear Driving Force; MBTSA, Moving Bed Temperature Swing Adsorption; PSA, Pressure Swing Adsorption; TSA, Temperature Swing Adsorptio; VSA, Vacuum Swing Adsorption.

* Corresponding author at: NTNU - Norwegian University of Science and Technology, Department of Energy and Process Engineering, Trondheim, Norway.
*E-mail address:* giorgia.mondino@sintef.no (G. Mondino).

https://doi.org/10.1016/j.ijggc.2022.103685
Received 25 May 2021; Received in revised form 22 April 2022; Accepted 27 April 2022
Available online 13 May 2022

**Nomenclature**

*Latin symbols*

| | |
|---|---|
| $a$ | Fitting constant - |
| $a'$ | Particle specific area $m^2/m^3$ |
| $A_i$ | First single-component Virial coefficients kg/mol |
| $A_{ij}$ | First multi-component Virial coefficients kg/mol |
| $A_{0,i}$ | Fitting constants of the first Virial coefficients kg/mol |
| $A_{1,i}$ | Fitting constants of the first Virial coefficients K kg/mol |
| $A_{cf,s}$ | Cross-flow area of the sorbent side $m^2$ |
| $A_{cf,w}$ | Cross-flow area of the water side $m^2$ |
| $A_s$ | Heat transfer area of the sorbent side $m^2$ |
| $A_w$ | Heat transfer area of the water side $m^2$ |
| $b$ | Fitting constant - |
| $B_i$ | Second single-component Virial coefficients $kg^2/mol^2$ |
| $B_{ijk}$ | Second multi-component Virial coefficients $kg^2/mol^2$ |
| $B_{0,i}$ | Fitting constants of the second Virial coefficients $kg^2/mol^2$ |
| $B_{1,i}$ | Fitting constants of the second Virial coefficients K $kg^2/mol^2$ |
| $Bi_i$ | Biot number of the adsorbent particles for component $i$ - |
| $c_{p,f}$ | Specific heat capacity of the heating/cooling fluid J/kg K |
| $c_{p,g}$ | Specific heat capacity of the gas mixture J/kg K |
| $c_{p,pk}$ | Specific heat capacity of packing material J/kg K |
| $c_{p,s}$ | Specific heat capacity of the adsorbent J/kg K |
| $c_{p,t}$ | Specific heat capacity of the heat exchanger tubes J/kg K |
| $c_{p,w}$ | Specific heat capacity of water J/kg K |
| $\hat{c}_p$ | Molar heat capacity of the gas mixture at constant pressure J/mol K |
| $\hat{c}_v$ | Molar heat capacity of the gas mixture at constant volume J/mol K |
| $C_i$ | Molar concentration of component $i$ in the gas phase mol/$m^3$ |
| $C_{p,i}$ | Molar concentration of component $i$ in the macropores mol/$m^3$ |
| $C_T$ | Total molar concentration of the gas phase mol/$m^3$ |
| $d_p$ | Particle diameter m |
| $d_{t,ext}$ | Equivalent external diameter of the tubes m |
| $d_{t,int}$ | Internal diameter of the tubes m |
| $D_c^0$ | Micropore limiting diffusivity at infinite temperature $m^2/s$ |
| $D_{ij}$ | Binary molecular diffusivity of components $(i,j)$ $m^2/s$ |
| $D_{Kn,i}$ | Knudsen diffusivity of component $i$ $m^2/s$ |
| $D_{m,i}$ | Molecular diffusivity of component $i$ $m^2/s$ |
| $D_{p,i}$ | Macropore diffusivity of component $i$ $m^2/s$ |
| $D_{z,i}$ | Axial dispersion coefficient of component $i$ $m^2/s$ |
| $E_{a,i}$ | Activation energy of micropore diffusion of component $i$ J/mol |
| $h_{gs}$ | Heat transfer coefficient between gas and solid W/$m^2$ K |
| $h_{ft}$ | Heat transfer coefficient between fluid and tube walls W/$m^2$ K |
| $h_{gt}$ | Heat transfer coefficient between gas and tube walls W/$m^2$ K |
| $h_s$ | Heat transfer coefficient on the sorbent side W/$m^2$ K |
| $h_w$ | Heat transfer coefficient on the water side W/$m^2$ K |
| $J_s$ | Sorbent mass flux kg/$m^2$ s |
| $k_{f,i}$ | Film mass transfer coefficient of component $i$ m/s |
| $k_g$ | Thermal conductivity of the gas mixture W/m K |
| $k_w$ | Thermal conductivity of water W/m K |
| $K_{H,i}$ | Henry's law constant of component $i$ mol/kg Pa |
| $K_{H,i}^{\infty}$ | Henry's law constant at infinite temperature mol/kg Pa |
| $l_t$ | Length of a single tube m |
| $l_{t,tot}$ | Total length of the tubes m |
| $L_x$ | Tube length along flow direction m |
| $L_z$ | Section length along vertical axis m |
| $\dot{m}$ | Mass flow rate mol/s |
| $\dot{m}_s$ | Mass flow rate of sorbent mol/s |
| $\dot{m}_w$ | Mass flow rate of water mol/s |
| $M_w$ | Molecular weight kg/mol |
| $\dot{n}$ | Molar flow rate mol/s |
| $N_{mod}$ | Number of heat exchanger modules - |
| $N_{pass}$ | Number of passes per module - |
| $N_t$ | Number of tubes per module - |
| $N_{t,pass}$ | Number of tubes per pass - |
| Nu | Nusselt number - |
| $P$ | Total pressure of the gas mixture Pa |
| $P_i$ | Partial pressure of component $i$ Pa |
| Pe | Péclet number - |
| Pr | Prandtl number - |
| $q_i$ | Adsorbed concentration of component $i$ mol/kg |
| $q_i^*$ | Adsorbed concentration of component $i$ at equilibrium mol/kg |
| $\dot{Q}$ | Heat flow rate W |
| $r_c$ | Micropore radius m |
| $r_p$ | Particle radius m |
| $r_{pore}$ | Macropore radius m |
| $r_{t,int}$ | Internal radius of the tubes m |
| $R$ | Ideal gas constant J/K mol |
| $R_t$ | Heat transfer resistance of the tubes K/W |
| $R_{tot}$ | Total heat transfer resistance K/W |
| $R_s$ | Heat transfer resistance on the sorbent side K/W |
| $R_w$ | Heat transfer resistance on the water side K/W |
| Re | Reynolds number - |
| $s_{CO_2/N_2}$ | Adsorbent selectivity of carbon dioxide over nitrogen - |
| $s_{t,ext}$ | External side length of the tubes m |
| $Sc_i$ | Schmidt number of component $i$ - |
| $Sh_i$ | Sherwood number of component $i$ - |
| $t$ | Time s |
| $t_{cycle}$ | Cycle time of the MBTSA process s |
| $T$ | Temperature of the gas K |
| $T_f$ | Temperature of the heating/cooling fluid K |
| $T_s$ | Temperature of the sorbent particles K |
| $T_t$ | Temperature of the heat exchanger tubes wall K |
| $T_w$ | Temperature of the water K |
| $u$ | Superficial velocity of the gas m/s |
| $u_f$ | Velocity of the heating/cooling fluid m/s |
| $v_s$ | Velocity of the adsorbent m/s |
| $v_w$ | Velocity of water m/s |
| $Y_i$ | Molar fraction of component $i$ - |
| $z$ | Coordinate along the section height m |

*Greek symbols*

| | |
|---|---|
| $\alpha_{gt}$ | Ratio of external surface area of tubes to gas-solid volume $m^2/m^3$ |
| $\alpha_{t,ext}$ | Ratio of external surface area of tubes to fluid volume $m^2/m^3$ |
| $\alpha_{t,int}$ | Ratio of internal surface area of tubes to fluid volume $m^2/m^3$ |
| $\Delta H_i$ | Heat of adsorption of component $i$ J/mol |
| $\Delta T_{LM}$ | Logarithmic mean temperature difference K |
| $\varepsilon$ | Column void fraction - |
| $\varepsilon_p$ | Particle porosity - |
| $\lambda_g$ | Axial heat dispersion coefficient of the gas mixture W/m K |
| $\lambda_{pk}$ | Axial heat dispersion coefficient of the packing W/m K |
| $\mu_g$ | Dynamic viscosity of the gas mixture Pa s |
| $\mu_w$ | Dynamic viscosity of water Pa s |
| $\xi$ | Packing porosity factor - |

| | | | |
|---|---|---|---|
| $\rho_f$ | Density of the heating/cooling fluid kg/m$^3$ | $\rho_w$ | Density of water kg/m$^3$ |
| $\rho_g$ | Density of the gas mixture kg/m$^3$ | $\sigma_{ij}$ | Lennard-Jones parameter of binary diffusivity m |
| $\rho_p$ | Density of the adsorbent particles kg/m$^3$ | $\tau_p$ | Particle tortuosity - |
| $\rho_{pk}$ | Density of the packing kg/m$^3$ | $\Omega_{D_{ij}}$ | Dimensionless collision integral of binary diffusivity - |
| $\rho_t$ | Density of the heat exchanger tubes kg/m$^3$ | | |

plants, the $CO_2$ has to be purified from low-concentration, low-pressure and high volume flow rate flue-gases and regeneration via temperature swing seems to be the most appropriate option (Bui et al., 2018; Ruthven, 1984; Wankat, 2006). The main reason for this is that TSA processes have minimal electric power consumption compared to PSA/VSA and offer the possibility to exploit waste heat from the power plant to regenerate the sorbent (Plaza and Rubiera, 2019).

In conventional TSA processes, the adsorbent is normally shaped as beads or pellets and packed in a series of columns that cyclically alternate between the adsorption and regeneration steps. One of the main drawbacks of fixed bed processes in applications involving large flow rates, such as post-combustion capture, is the high pressure drop occurring across the packed-bed, unless the adsorbent pellets are replaced by especially shaped adsorbents (e.g., honeycomb monolith, hollow fibers, spaced sheets) (Akhtar et al., 2014; Farmahini et al., 2021; Masala et al., 2017; Rezaei and Webley, 2010).

Another important factor hampering the commercialization of TSA systems for post-combustion $CO_2$ capture is that a large temperature swing is often required (Morales-Ospino et al., 2021; Zanco et al., 2018) to achieve the demanding product specifications in terms of both $CO_2$ purity and recovery (Joss et al., 2017). These large temperature swings do not only imply high energy penalties and parasitic losses, but also lead to long cycle times due to the poor heat transfer within the packed bed (Bonjour et al., 2004; Plaza et al., 2017; Zanco et al., 2021). This, in turn, results in large sorbent inventories, low process productivity, and large system footprints, which makes conventional TSA processes less competitive with respect to other post-combustion technologies (Bonjour et al., 2005; Rezaei and Webley, 2010; Zanco et al., 2021; 2017).

One way to overcome the aforementioned challenges is by performing the adsorption-desorption cycle in a moving bed system, rather than in the traditional fixed bed configuration (Knaebel, 2005). In the moving bed process, the temperature swing is achieved by circulating the adsorbent through sections at different temperatures. Each of these sections has a specific purpose and corresponds to a different step: adsorption, desorption and cooling. In contrast with fixed bed processes in which the same column is operated at variable conditions according to the cycle schedule, each section of the moving bed system can be designed and operated according to its specific purpose. This offers interesting opportunities for system optimization, aiming, for example, to reduce the pressure drop within the adsorption section, or to enhance heat transfer in the desorption and cooling sections, so that a more compact design and higher productivity can be achieved.

Furthermore, the MBTSA offers the possibility to internally recover part of the heat needed for sorbent regeneration and thus reduce the external energy duty of the process (Kim et al., 2013; Knaebel, 2005; Morales-Ospino et al., 2021).

Another major feature distinguishing moving bed from fixed bed processes is that the former can be operated at steady state, avoiding complex cycle scheduling (Kim et al., 2013; Plaza et al., 2017) and the parasitic losses associated with intermittent heating/cooling of the heat exchanger walls (Bonjour et al., 2005; 2004). The possibility to operate in steady state is also an advantage in terms of process control and integration (Kim et al., 2013), which is particularly relevant within post combustion applications where: (i) the flow rate and composition of flue gases from the upstream power plant can vary over time (Montañés et al., 2018; Rúa et al., 2020), (ii) the power cycle can be appositely modified to supply the heat required by the capture process (Mondino et al., 2019)

The concept of moving bed was first introduced in the '40s by Berg (1945) for fractionating hydrocarbons. Only recently the same concept has been applied for $CO_2$ capture purposes, first by Knaebel (2005) who suggested the use of hot flue gas for indirect sorbent heating, and later by Hornbostel and co-workers (Hornbostel, 2016; Hornbostel et al., 2013; 2015), who tested a large bench scale moving bed system employing steam for direct heating of the adsorbent. Pilot-scale design and testing of a moving-bed process for $CO_2$ capture was performed also by Okumura et al. (2014, 2017), who used an amine impregnated adsorbent regenerated by low temperature steam in a direct-contact type heat exchanger. One of the main advantages of direct sorbent heating is that it is possible to achieve fast heat transfer rates due to intense mixing between sorbent particles and heating fluid. In addition, the steam helps to regenerate the sorbent by acting as a sweeping gas and as a concentration swing promoter, lowering the partial pressure of $CO_2$. However, this type of configuration prevents the use of sorbents materials that are incompatible with the heat transfer fluid and compromises the use of internal heat recovery, which is crucial to minimize the process energy use. In this context, the group of Kim et al. (2013), Kim et al. (2014), Son et al. (2014) proposed a moving bed process with an internal heat integration scheme, where part of the energy required for sorbent regeneration is recovered from the heat generated during the adsorption step using indirect-contact heat exchangers. The same type of indirect-contact heat exchanger for MBTSA processes was employed in the recent study carried out by Morales-Ospino et al. (2021), who confirmed that internal heat recovery is crucial to limit the process energy penalty.

The success of this heat integration is largely dependent on the performance of the indirect-contact heat exchanger employed to provide and remove heat from the sorbent. In particular, the estimation of the sorbent-side heat transfer coefficient is crucial for the design of the MBTSA system because it represents the limiting thermal resistance between the gas/adsorbent phases and the heating/cooling fluid. The convective heat transfer to the flowing sorbent is determined by several factors, including the flow pattern, particle mixing, contact area between sorbent and hot surfaces, as well as the sorbent residence time. The effective heat transfer is therefore affected not only by the geometry of the system (e.g., tube arrangements and shape, hydraulic diameters, pitching) or operating conditions (e.g., temperatures of heating/cooling fluid, flow rates), but also by specific properties of the bulk solid that influence its flowability (e.g., particle shape, size, density). Several studies investigated the heat transfer mechanisms in moving bed heat exchangers employing bulk solids as working fluid, both computationally (Campbell, 1990; Isaza et al., 2015; Lee et al., 1998) and experimentally (Al-Ansary et al., 2012; Baird et al., 2008; Baumann and Zunft, 2015; Niegsch et al., 1994). As an example, the recent works by Qoaider et al. (2017), Dai et al. (2020) analyzed how different materials, including glass beads, corundum, sand, basalt or mixtures thereof, result in different flow characteristics. Other studies focused on different system geometries and configurations, considering for example moving packed beds with and without gas flow (Baird et al., 2008), or comparing horizontal tubes, vertical tubes, parallel plates, and finned tubes (Al-Ansary et al., 2012). The influence of the tube shapes on the local heat transfer has also been investigated by Tian et al. (2020), who compared circular cross-sectioned tubes with elliptical shaped ones. One of the conclusions from the surveyed literature is that the convective

heat transfer coefficient of flowing solid particles in moving bed heat exchangers is case-specific and hard to estimate without experimental data (Obuskovic, 1988).

Another factor hindering the development of the MBTSA technology is the lack of an established method to design a process for a given flue gas specification. The design of an MBTSA system is a complex task that involves a large number of inter-related process parameters such as the choice of adsorbent material, process configuration, size and geometry of the different components, and operating conditions. In this context, process modelling and simulation is an essential tool for the conceptualization and analysis of new MBTSA systems. Provided that the model captures all relevant physical mechanisms, process simulations can be used to evaluate the system performance under different conditions. This, in turn, can help the designer to gain a better understanding of the process and serve as a basis to improve the design until the desired performance targets are met. In view of these advantages, process simulation has been a popular tool for the design of post-combustion PSA/VSA (Farmahini et al., 2021; Krishnamurthy et al., 2014; Liu et al., 2011) and TSA cycles (Joss et al., 2017; Lillia et al., 2018; Plaza et al., 2017). By contrast, modeling and simulation of MBTSA processes has lagged behind due to the early stage of development of this technology. In fact, only a handful of recent computational studies attempted to design and evaluate the performance of the MBTSA process for $CO_2$ capture in coal-fired power plants (Kim et al., 2013; Mondino et al., 2017; Morales-Ospino et al., 2021; Son et al., 2014) and natural gas combined cycle power plants (Mondino et al., 2019; 2020). However, to the knowledge of the authors', the utilization of the MBTSA technology for $CO_2$ capture in waste-to-energy plants has not been studied yet.

The aim of the present work is to design and evaluate an MBTSA process for capturing $CO_2$ from an industrial-scale waste-to-energy power plant. To assess the technology with realistic parameter values, we have measured heat transfer coefficients in the heating section of a new MBTSA demonstrator unit using activated carbon spheres with 0.7 mm diameter. In addition, a detailed computational model previously developed by the authors (Mondino et al., 2020) has been extended to include the experimentally measured heat transfer coefficients and to account for the internal heat recovery achieved by coupling the preheating and precooling sections. The feasibility of the proposed MBTSA process is evaluated based on different performance indicators including system footprint, energy duty, $CO_2$ separation performance, and process productivity.

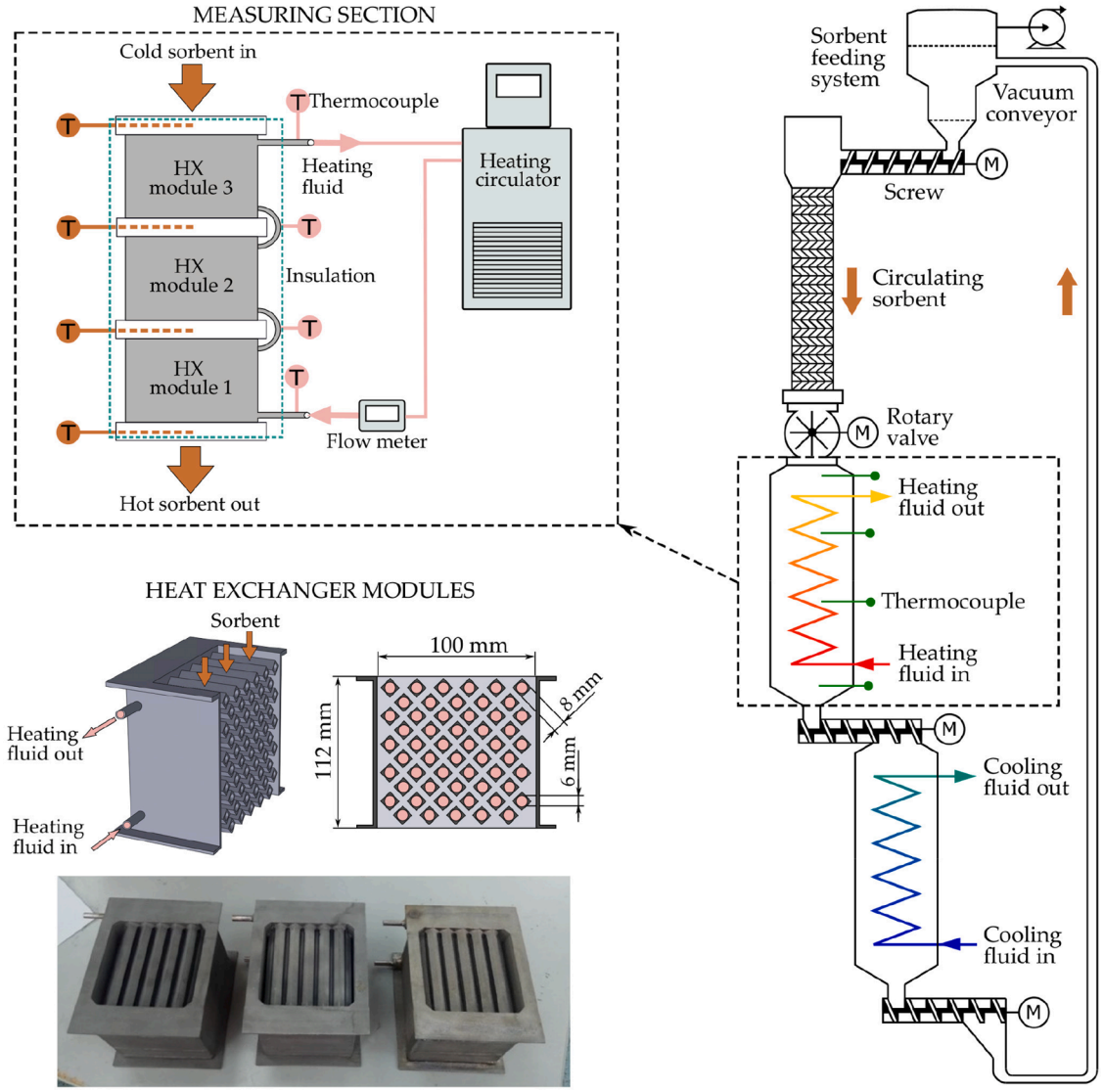


**Fig. 1.** Experimental set-up used for heat transfer measurements: schematic diagram of the lab-scale moving bed (right), details on the measuring section (top left) and heat exchanger modules with a sectioned three-dimensional view, a cross-section and a picture of the three modules (bottom left).

## 2. Heat transfer measurements

A series of experiments were carried out in a lab-scale apparatus replicating a full MBTSA process with the aim to analyze the heat transfer performance of the desorption section.

### 2.1. Experimental apparatus

The MBTSA apparatus, schematically shown in Fig. 1, is composed of three main sections, namely the adsorption, the desorption and the cooling sections, through which the adsorbent circulates in a continuous manner. The adsorbent is released into the adsorption section at a controlled flow rate from a feeding system placed at the top (ZD22B Standard Feeder, ThreeTec, Switzerland). The adsorption section consists of a 1.5 m high, 5 cm internal diameter polycarbonate column filled with structured packing (Mellapack$^{TM}$ 500Y, Sulzer, Switzerland) that ensures uniform distribution of the sorbent flow.

After passing through the adsorption section, the sorbent enters a rotary valve (ACS valve, CI series) activated by a three-phase induction motor connected to the power supply by a WEG frequency inverter (CFW500 vector inverter/series). The rotary valve discharges the sorbent into the desorption section indicated as "measuring section" in Fig. 1. This part consists of a series of three heat exchanger modules (shell-and-tube), in which the sorbent is indirectly heated by a thermal fluid. More specifically, the adsorbent moves downwards in the shell-side of the heat exchanger while the heating media flows within the horizontal tubes in a cross-flow mode. In addition, the lateral surfaces of the heat exchanger modules are insulated with a glass wool layer to limit the heat losses to the surroundings.

Each heat exchanger module contains a bundle of 55 horizontal tubes through which the heating fluid is distributed in a multi-pass configuration. As shown on the bottom left side of Fig. 1, the tubes present an inner circular cross section (6 mm in diameter) and an outer squared cross section with a square side of 8 mm. Such configuration and tube shape were adopted to ensure good contact between the sorbent particles and the heating surface, enhancing the heat transfer rate. In particular, staggered horizontal tube arrangements promote a better particle mixing in comparison with vertical tubes or plate configurations (Baumann and Zunft, 2015; Takeuchi, 1996; Tian et al., 2020), especially when the tube pitch is narrow (Baumann et al., 2014). Furthermore, using a squared cross-section alleviates the local formation of stagnant and void zones above and below the tubes, respectively. This phenomenon typically occurs on circular tubes and limits the performance of the heat exchanger (Baumann and Zunft, 2015; Niegsch et al., 1994). The numerical values of the geometrical parameters of the heat exchanger are listed in Table 1.

Water is used as thermal fluid, supplied by a SE-6 JULABO heating circulator. The temperature of the water at the heat exchanger inlet is controlled by adjusting the set point on the heating circulator. The flow rate is measured with a turbine flow meter (F110P-AU model, HP series, KEM - Germany) installed between the heating circulator and the heat exchanger. The mass flow rate cannot be directly controlled as it depends on the balance between the pressure drop in the circuit and the charateristic of the Julabo circulator pump.

The sorbent temperature is measured with four thermocouples located at different positions within the heat exchangers, see Fig. 1 (top left). The thermocouples are installed within the spacers separating the modules to ensure a good contact with the bulk of the sorbent flow. Four additional thermocouples are used to measure the water temperature at the inlet and outlet of the measuring section and between the heat exchanger modules. All thermocouples are connected to a data acquisition system to record the temperature data in a LabVIEW interface LabVIEW. Moreover, a series of powder level sensors are installed within the spacers separating the heat exchanger modules and connected to the LabVIEW program for monitoring the level of adsorbent inside the heat exchangers and ensure that the bed is packed during operation.

**Table 1**
Geometry and material properties of the heat exchanger used for the heat transfer measurements.

| Parameter | Symbol | Unit | Value |
|---|---|---|---|
| Number of modules | $N_{mod}$ | - | 3 |
| Number of tubes per module | $N_t$ | - | 55 |
| Number of passes (water side)[a] | $N_{pass}$ | - | 5 |
| Number of tubes per pass (water side) | $N_{t,pass}$ | - | 11 |
| Internal tube diameter | $d_{t,int}$ | m | 0.006 |
| External tube square side | $s_{t,ext}$ | m | 0.008 |
| Single tube length | $l_t$ | m | 0.1 |
| Total tube length | $l_{t,tot}$ | m | 16.50 |
| Heat transfer area - water side | $A_w$ | $m^2$ | 0.311 |
| Heat transfer area - sorbent side | $A_s$ | $m^2$ | 0.528 |
| Cross flow area - sorbent side[b] | $A_{cf,s}$ | $mm^2$ | 6857 |
| Cross flow area - water side[c] | $A_{cf,w}$ | $mm^2$ | 311 |
| Tubes material | - | - | TiAl6V4 |
| Specific heat capacity of TiAl6V4 | $c_{p,t}$ | J/kg K | 526 |
| Thermal conductivity of TiAl6V4 | $k_t$ | W/m K | 6.6 |
| Density of TiAl6V4 | $\rho_t$ | $kg/m^3$ | 4420 |

[a] The flow is directed into separate passes by four baffles placed in the lateral heads.
[b] Calculated as the volume available for the sorbent flow divided by the module height.
[c] Calculated as the internal cross section of a single tube multiplied by the number of tubes per pass.

The bottom outlet of the heating section is connected to an adjustable transport screw driven by a stepper motor (M1343031, LAM Technologies) that discharges the sorbent into the cooling section. The speed of the screw is adjusted through the LabView program while monitoring the powder level indicators so that the level of adsorbent inside the heat exchanger can be kept as desired.

The cooling section is similar to the heating one, but has only two modules and employs water as cooling media supplied by a Julabo CORIO™ CD-300F Refrigerated Circulator. After passing through the cooling section, the sorbent finally reaches a collector funnel at the bottom of the unit from which it is transported back to the top feeder by means of a vacuum conveyor system.

### 2.2. Experimental procedure

The heat transfer measurements were carried out using a commercial activated carbon shaped as 0.5–1.0 mm spherical beads supplied by Blücher (Germany). The physical properties of the adsorbent are summarized in Table 2.

The system was loaded with approximately 10 kg of adsorbent. As previously mentioned, the adsorbent flow rate is controlled by the upper feeding system through a double screw that can be operated at different rotational rates. As the actual feeding rate does not only depend on the apparatus specifications, but also on the type of sorbent material and its flowing properties, the feeding system was calibrated prior to the experiments. To this aim, the sorbent flow rates were measured at different rotating speeds of the feed screw within the experimental range (7–24 g/

**Table 2**
Physical properties of the adsorbent material.

| Parameter | Value | Unit |
|---|---|---|
| Adsorbent type | Activated carbon* | – |
| Particle shape | Spherical beads | – |
| Particle diameter† | 0.7 | mm |
| Bulk density | 452 | $kg/m^3$ |
| Particle density† | 904 | $kg/m^3$ |
| Heat capacity† | 880 | kJ/kg K |
| Particle porosity† | 0.50 | – |

* Provided by Blücher (Germany). † Input value for the MBTSA simulations.

s).

All experimental data were collected upon reaching steady state, which was assessed by monitoring the system temperatures via the LabVIEW interface. The sorbent feeding system was activated starting from the lowest flow rate and operated for several minutes until a new steady state was reached. At this point, the temperature measurements were recorded in LabVIEW with a frequency of 30 readings per minute. The sorbent flow rate was then changed to the next set point and the procedure was repeated. Each data point was obtained by averaging the readings over a period of least 5 min to reduce the influence of instantaneous random fluctuations.

### 2.3. Determination of the heat transfer coefficient

The heat transfer coefficient is determined from the governing equations of the heat exchangers. The main assumptions underlying this analysis are: steady-state operating conditions, one-dimensional flow, negligible changes in the potential and kinetic energy of the fluids, constant transport properties, no fouling on internal heat exchanger surfaces, uniform heat transfer coefficients, and negligible heat loss to the surroundings. The latter assumption was verified by estimating the heat loss due to the natural convection of air on the vertical surfaces exposed to the surrounding. Based on the actual temperature of the exposed insulation layer and the room temperature, the heat loss was estimated to be less than 1 % of the total heat transfer rate in all cases.

Under the assumption of negligible heat loss, the heat transfer from the water is equal to the heat transfer to the sorbent. If, in addition, the specific heat of water is assumed to be constant, the heat flow rate can be calculated from the measured data according to:

$$\dot{Q} = \dot{m}_w c_{p,w} \left(T_{w,in} - T_{w,out}\right), \tag{1}$$

where the subscript w stands for water.

Using the mean logarithmic temperature difference approach (Cengel et al., 1998), the heat transfer rate can be related to the heat transfer resistances as:

$$\dot{Q} = \frac{\Delta T_{LM}}{R_{tot}}, \tag{2}$$

where $R_{tot}$ is the total heat transfer resistance and $\Delta T_{LM}$ is the logarithmic mean temperature difference for the counter-flow arrangement. The total thermal resistance, $R_{tot}$, is the sum of the contributions due to internal convection (water-side), conduction across the tube walls, and external convection (sorbent-side). The average heat transfer coefficient between the flowing sorbent and the tube walls, $h_s$, can be solved from:

$$R_{tot} = R_w + R_t + R_s = \frac{1}{A_w h_w} + \frac{\ln\left(d_{t,ext}/d_{t,int}\right)}{2\pi k_t l_{t,tot}} + \frac{1}{A_s h_s}, \tag{3}$$

where the subscript t stands for tubes and s for sorbent, whereas $A_s$ is the heat transfer area on the sorbent side, given by:

$$A_s = 4 s_{t,ext}\, l_t\, N_{mod}\, N_t. \tag{4}$$

Concerning the internal convective resistance (water side), the heat transfer area $A_w$ is calculated directly from the system geometry as:

$$A_w = 2\pi r_{t,int}^2\, l_{t,tot}, \tag{5}$$

where $l_{t,tot}$ is the total length of tubes in the heat exchanger and $r_{t,int}$ is the internal tube diameter. Moreover, the internal heat transfer coefficient, $h_w$, is estimated from an empirical correlation. As the water flow is laminar in all the tests (Reynolds numbers between 1178–1638), the following correlation for internal laminar flow was adopted (Cengel et al., 1998):

$$\mathrm{Nu} = \frac{h_w d_{t,int}}{k_w} = 3.66 + \frac{0.065\left(d_{t,int}/l_t\right)\mathrm{Re}\,\mathrm{Pr}}{1 + 0.04\left[\left(d_{t,int}/l_t\right)\mathrm{Re}\,\mathrm{Pr}\right]^{2/3}} \tag{6}$$

The water conductivity, $k_w$, and the dimensionless numbers appearing in the correlation were evaluated at the bulk mean water temperature (i.e., arithmetic average of the temperature at the inlet and outlet).

Lastly, the tube walls resistance, $R_t$, was directly calculated from the thermal properties of the tube material (TiAl6V4 alloy) and the system geometry. For this purpose, the square profile of the tubes (with a side length $s_{t,ext}$) was converted into an equivalent circular profile (with diameter $d_{t,ext}$) with the same cross-sectional area as the actual profile.

### 2.4. Experimental results

An example of the collected temperature data is shown in Fig. 2, where the points in the plots correspond to the temperatures sensed by the thermocouples, as specified in the schematic diagram on the right side. It was observed that, in all the experiments performed, the largest adsorbent temperature gain is achieved within the first module, while only a small fraction of heat is exchanged in the second module and almost no heat in the third one. Furthermore, the change in temperature experienced by the water, is only a few degrees in the first module and almost negligible in the second and third ones. It was therefore decided to estimate the heat transfer coefficient using only the data corresponding to the first module, where the majority of the heat exchange takes place and the results have the least uncertainty.

The numerical values of the measured temperatures and the thermal parameters used to estimate the heat transfer coefficient are reported in Table 3. The estimated heat transfer rate, $\dot{Q}$, ranged between 249 W and 629 W, corresponding to tests 4 and 9, respectively. With regards to the thermal resistances, the convection on the sorbent-side was always the dominating resistance, ranging between 72 and 82% of the total thermal resistance, while the conductive resistance of the tube walls ranged between 1.8 and 2.7%.

The convective heat transfer coefficient on the sorbent side was computed for each operating point solving Eq. (3), and the results were plotted against the velocity of the solid particles in Fig. 3. As expected, the heat transfer coefficient increases with the solid velocity (Al-Ansary et al., 2012; Baumann and Zunft, 2015; Niegsch et al., 1994), while no dependence was observed on the solid temperature. The measured heat transfer coefficients ranged between 69 and 117 W/m$^2$ K with an uncertainty below 8% in all cases, which was evaluated using the law of propagation of uncertainty (Farrance and Frenkel, 2012). The trend of the experiments suggests that even higher values might be achieved by operating the system at higher solid velocities. However, this hypothesis could not be verified due to the limitations of the experimental apparatus.

In order to correlate the experimental results, the heat transfer coefficient and solid velocity were expressed in terms of dimensionless quantities. The dependence of the heat transfer coefficient on: (i) gas thermal conductivity, (ii) bulk density, (iii) sorbent heat capacity, (iv) solid velocity, and (v) tube external side can be expressed as:

$$f\left(h_s,\, k_g,\, \rho_b,\, c_{p,s},\, v_s,\, s_{t,ext}\right) = 0. \tag{7}$$

Since this relationship involves 6 variables and 4 physical dimensions (i.e., time, length, mass, and temperature), dimensional analysis yields two independent dimensionless groups:

$$g(\mathrm{Nu},\, \mathrm{Pe}) = 0, \tag{8}$$

where

$$\mathrm{Nu} = \frac{h_s s_{t,ext}}{k_g} \tag{9}$$

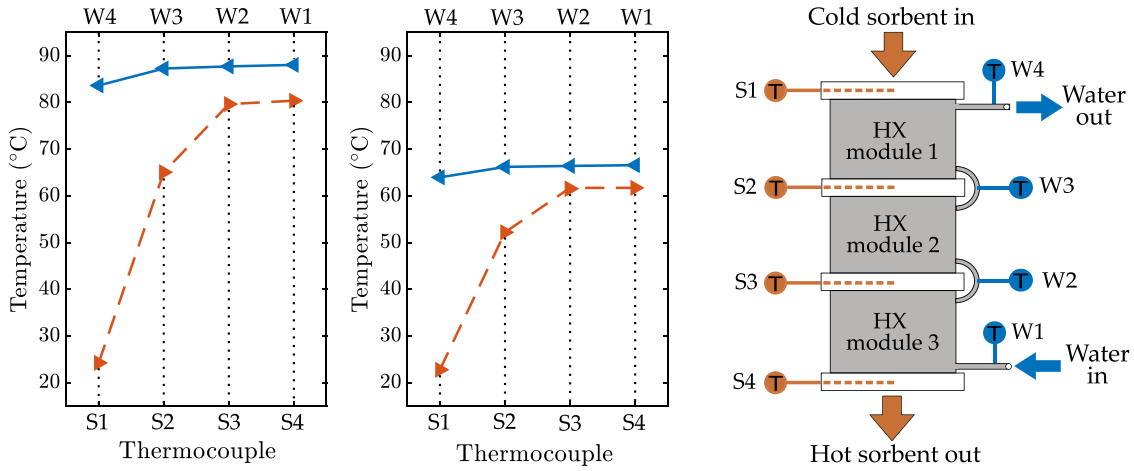


**Fig. 2.** On the left, example of experimental results obtained for two test runs (2, left and 4, right): Plot of the measured sorbent (orange) and water (blue) temperatures. On the right, schematic diagram of the experimental set-up indicating the position of each thermocouple. (For interpretation of the references to colour in this figure legend, the reader is referred to the web version of this article.)

is the Nusselt number and

$$\mathrm{Pe} = \frac{\rho_b c_{p,s} v_s s_{t,ext}}{k_g} \tag{10}$$

is the Péclet number. The Nusselt and Péclet numbers can be interpreted as the dimensionless heat transfer coefficient and solid velocity, respectively. Using these dimensionless numbers, the experimental results were correlated by means of least-squares regression analysis, and the following equation was obtained:

$$\mathrm{Nu} = a\,\mathrm{Pe}^b = 0.808\,\mathrm{Pe}^{0.445}. \tag{11}$$

This correlation is used to estimate the heat transfer rate within the full-scale MBTSA model described in the following section. As shown in Fig. 3 (right), the relative deviation between the heat transfer coefficients determined experimentally and the values predicted by Eq. (11) is below 5% for all cases. In addition, the coefficient of determination obtained from the regression analysis is $R^2 = 0.995$. This suggests that the proposed correlation is adequate to predict the heat transfer coefficient for flowing adsorbent particles within cross-flow shell-and-tube heat exchangers, provided that they are geometrically similar and operated within the range of particle velocities considered in these experiments.

In addition, Fig. 3 (left) compares the heat transfer coefficients measured in this work against those reported by Obuskovic (1988) for a single tube immersed in a moving bed of solid particles. The heat transfer coefficients obtained for the activated carbon particles considered in this work are comparable with those obtained by Obuskovic (1988) for glass and sand particles of different diameters. In addition, the variation of the heat transfer coefficient with the velocity of the solid particles follows the same trend as the data from Obuskovic (1988). In particular, the exponent of the Péclet number obtained in the present work ($b = 0.455$), see Eq. (11), agrees well with the exponent reported by Obuskovic (1988) for their low-velocity experiments ($b = 0.4$), and with the theoretical value suggested by Mickley and Fairbanks (1955) for an homogeneous moving bed of infinitesimally small particles ($b = 0.5$).

Finally, the heat transfer coefficients measured in this work are significantly higher than those typically encountered in fixed bed configurations. For example, Marx et al. (2016) reported heat transfer coefficients between 20 and 40 W/m$^2$ K when performing TSA experiments on a indirectly-heated packed bed filled with a zeolite 13X adsorbent shaped as spherical beads with diameters between 1.6 and 2.0 mm. Similarly, Bonjour et al. (2002) obtained heat transfer values up to 50 W/m$^2$ K when measuring the heat transfer performance of a coaxial packed bed heat exchanger filled with activated carbon beads of 0.65 mm mean diameter. This confirms that the moving bed configuration has the potential to address one of the main limitations of the fixed bed TSA process, namely, the low productivity due to the slow heating and cooling of the adsorbent.

## 3. Application of the MBTSA process to a waste-to-energy plant

### 3.1. Case study definition

The second part of this study considers the application of the MBTSA process to capture $CO_2$ from a Combined Heat and Power (CHP) waste-to-energy plant with a net power output of 16.8 $MW_{el}$ and a thermal output of 64.6 $MW_{th}$. The power plant was modeled in Thermoflex software Thermoflow Version 27 using a built-in waste-to-energy plant model. The flue gas specification required to design the MBTSA process were obtained by simulating the plant at its nominal operating point. In order to reduce the computational effort of the MBTSA simulations, the composition of the exhaust gas was simplified to a binary mixture of $N_2$ and $CO_2$, assuming that: (i) the flue gas is dried prior to the capture process, and (ii) $O_2$ and Ar behave similarly to $N_2$ in terms of adsorption equilibrium and kinetics (Plaza et al., 2014; 2017). The resulting flue gas specifications, used as input for designing and simulating the MBTSA process, are listed in Table 4.

### 3.2. Adsorbent material

The adsorbent used for the case study was the same activated carbon employed in the heat transfer experiments.

The physical properties of the adsorbent used as basis for the MBTSA process simulations are summarized in Table 2.

In addition, the adsorption equilibrium data for $CO_2$ and $N_2$ were measured experimentally and fitted with a suitable adsorption isotherm model as described below.

Pure-component adsorption isotherms of $CO_2$ and $N_2$ were measured on a sample of the activated carbon using a volumetric adsorption apparatus (Belsorp Max, MicrotracBEL, Japan). The data were collected at six different temperatures between 30 and 150 °C. Prior to the measurements, overnight degassing of the sample was performed at 150 °C and vacuum conditions.

The experimental isotherms data were fitted with a Virial model truncated at its second term (Barrer, 1981; Grande et al., 2008):

**Table 3**
Overview of experimental results: measured data and calculated heat transfer parameters.

| | | | Test ID | | | | | | | | | | | | | | | |
|---|---|---|---|---|---|---|---|---|---|---|---|---|---|---|---|---|---|---|
| | | | 1 | 2 | 3 | 4 | 5 | 6 | 7 | 8 | 9 | 10 | 11 | 12 | 13 | 14 | 15 | 16 | 17 |
| **Sorbent** | | | | | | | | | | | | | | | | | | | |
| Flow rate | $\dot{m}_s$ | g/s | 7.72 | 7.72 | 16.99 | 7.34 | 16.82 | 16.82 | 21.70 | 23.29 | 23.84 | 7.73 | 11.78 | 12.28 | 21.92 | 12.60 | 23.02 | 21.65 | 21.65 |
| Mass flux | $J_s$ | kg/m$^2$s | 1.13 | 1.13 | 2.48 | 1.07 | 2.45 | 2.45 | 3.16 | 3.40 | 3.48 | 1.13 | 1.72 | 1.79 | 3.20 | 1.84 | 3.36 | 3.16 | 3.16 |
| Velocity | $v_s$ | mm/s | 2.49 | 2.49 | 5.48 | 2.37 | 5.43 | 5.43 | 7.00 | 7.51 | 7.69 | 2.49 | 3.80 | 3.96 | 7.07 | 4.07 | 7.43 | 6.98 | 6.98 |
| Inlet temp. | $T_{s,in}$ | °C | 25.1 | 24.2 | 26.4 | 22.7 | 24.9 | 26.7 | 27.7 | 28.8 | 26.4 | 21.2 | 24.4 | 22.6 | 26.9 | 23.2 | 25.9 | 31.0 | 27.5 |
| Outlet temp. | $T_{s,out}$ | °C | 66.2 | 65.1 | 55.8 | 52.2 | 45.5 | 46.0 | 43.5 | 52.0 | 51.1 | 66.6 | 60.8 | 59.0 | 53.5 | 48.2 | 41.2 | 45.8 | 43.2 |
| **Water** | | | | | | | | | | | | | | | | | | | |
| Inlet temp. | $T_{w,in}$ | °C | 87.5 | 87.3 | 85.7 | 66.2 | 65.3 | 65.3 | 64.7 | 84.7 | 84.6 | 87.3 | 86.7 | 86.4 | 84.9 | 65.7 | 64.2 | 64.9 | 64.5 |
| Outlet temp. | $T_{w,out}$ | °C | 84.2 | 83.6 | 80.6 | 64.0 | 62.0 | 62.1 | 61.2 | 79.2 | 78.9 | 83.7 | 82.4 | 81.8 | 79.4 | 62.8 | 60.5 | 61.7 | 61.0 |
| Flow rate | $\dot{m}_w$ | g/s | 27.65 | 25.09 | 25.21 | 26.57 | 26.58 | 26.58 | 26.59 | 26.51 | 26.51 | 25.67 | 25.68 | 25.69 | 25.70 | 27.07 | 27.09 | 27.08 | 27.09 |
| Velocity | $v_w$ | mm/s | 91.88 | 83.39 | 83.72 | 87.16 | 87.16 | 87.16 | 87.16 | 87.96 | 87.96 | 85.31 | 85.31 | 85.31 | 85.31 | 88.79 | 88.79 | 88.79 | 88.79 |
| Density | $\rho_w$ | kg/m$^3$ | 967 | 968 | 968 | 980 | 981 | 981 | 981 | 969 | 969 | 968 | 968 | 968 | 969 | 980 | 981 | 981 | 981 |
| Viscosity | $\mu_w$ | mPa s | 0.326 | 0.326 | 0.332 | 0.428 | 0.433 | 0.433 | 0.435 | 0.335 | 0.335 | 0.326 | 0.329 | 0.330 | 0.334 | 0.431 | 0.438 | 0.435 | 0.437 |
| Heat capacity | $c_{p,w}$ | J/kg K | 4202 | 4202 | 4201 | 4188 | 4187 | 4187 | 4187 | 4200 | 4200 | 4202 | 4202 | 4202 | 4201 | 4187 | 4187 | 4187 | 4187 |
| Conductivity | $k_w$ | W/m K | 0.671 | 0.671 | 0.670 | 0.656 | 0.656 | 0.656 | 0.655 | 0.670 | 0.670 | 0.671 | 0.671 | 0.671 | 0.670 | 0.656 | 0.655 | 0.655 | 0.655 |
| Reynolds | Re | - | 1638 | 1483 | 1466 | 1198 | 1185 | 1185 | 1178 | 1528 | 1526 | 1517 | 1507 | 1504 | 1485 | 1212 | 1193 | 1202 | 1197 |
| Prandtl | Pr | - | 2.04 | 2.04 | 2.08 | 2.73 | 2.77 | 2.77 | 2.78 | 2.10 | 2.10 | 2.04 | 2.06 | 2.06 | 2.09 | 2.75 | 2.80 | 2.78 | 2.79 |
| Nusselt | Nu | - | 5.19 | 5.08 | 5.09 | 5.17 | 5.17 | 5.17 | 5.17 | 5.14 | 5.14 | 5.11 | 5.11 | 5.11 | 5.11 | 5.19 | 5.19 | 5.19 | 5.19 |
| **Heat balance** | | | | | | | | | | | | | | | | | | | |
| Heat load | $\dot{Q}$ | W | 385.1 | 383.2 | 544.6 | 248.8 | 361.3 | 352.7 | 387.5 | 609.4 | 629.4 | 386.9 | 465.1 | 498.6 | 597.2 | 323.9 | 423.5 | 362.9 | 396.9 |
| Mean log $\Delta T$ | $\Delta T_{LM}$ | - | 37.05 | 37.82 | 40.87 | 25.21 | 27.54 | 26.54 | 26.88 | 40.91 | 42.25 | 37.82 | 39.74 | 41.28 | 41.07 | 27.09 | 28.37 | 24.41 | 26.92 |
| HTC water | $h_w$ | W/m$^2$K | 581.0 | 568.0 | 568.1 | 565.4 | 564.9 | 564.9 | 564.7 | 574.4 | 574.3 | 571.0 | 570.8 | 570.7 | 570.4 | 567.6 | 567.0 | 567.3 | 567.1 |
| HTC sorbent | $h_s$ | W/m$^2$K | 73.0 | 71.1 | 101.0 | 68.9 | 99.0 | 100.7 | 112.5 | 117.0 | 117.0 | 71.9 | 85.1 | 88.6 | 113.5 | 87.6 | 117.9 | 117.3 | 115.9 |
| **Thermal resistances** | | | | | | | | | | | | | | | | | | | |
| Total | $R_{tot}$ | K/kW | 96.19 | 98.70 | 75.03 | 101.30 | 76.24 | 75.27 | 69.38 | 67.13 | 67.13 | 97.76 | 85.45 | 82.79 | 68.76 | 83.65 | 66.98 | 67.25 | 67.83 |
| Water side | $R_w$ | K/kW | 16.60 | 16.98 | 16.98 | 17.06 | 17.07 | 17.07 | 17.08 | 16.79 | 16.79 | 16.89 | 16.90 | 16.90 | 16.91 | 16.99 | 17.01 | 17.00 | 17.01 |
| Tubes walls | $R_t$ | K/kW | 1.79 | 1.79 | 1.79 | 1.79 | 1.79 | 1.79 | 1.79 | 1.79 | 1.79 | 1.79 | 1.79 | 1.79 | 1.79 | 1.79 | 1.79 | 1.79 | 1.79 |
| Sorbent side | $R_s$ | K/kW | 77.80 | 79.93 | 56.26 | 82.45 | 57.37 | 56.40 | 50.51 | 48.54 | 48.54 | 79.08 | 66.76 | 64.10 | 50.06 | 64.86 | 48.18 | 48.46 | 49.03 |
| % water side | $R_w$ | % | 17.3 | 17.2 | 22.6 | 16.8 | 22.4 | 22.7 | 24.6 | 25.0 | 25.0 | 17.3 | 19.8 | 20.4 | 24.6 | 20.3 | 25.4 | 25.3 | 25.1 |
| % tubes walls | $R_t$ | % | 1.9 | 1.8 | 2.4 | 1.8 | 2.3 | 2.4 | 2.6 | 2.7 | 2.7 | 1.8 | 2.1 | 2.2 | 2.6 | 2.1 | 2.7 | 2.7 | 2.6 |
| % sorbent side | $R_s$ | % | 80.9 | 81.0 | 75.0 | 81.4 | 75.3 | 74.9 | 72.8 | 72.3 | 72.3 | 80.9 | 78.1 | 77.4 | 72.8 | 77.5 | 71.9 | 72.1 | 72.3 |

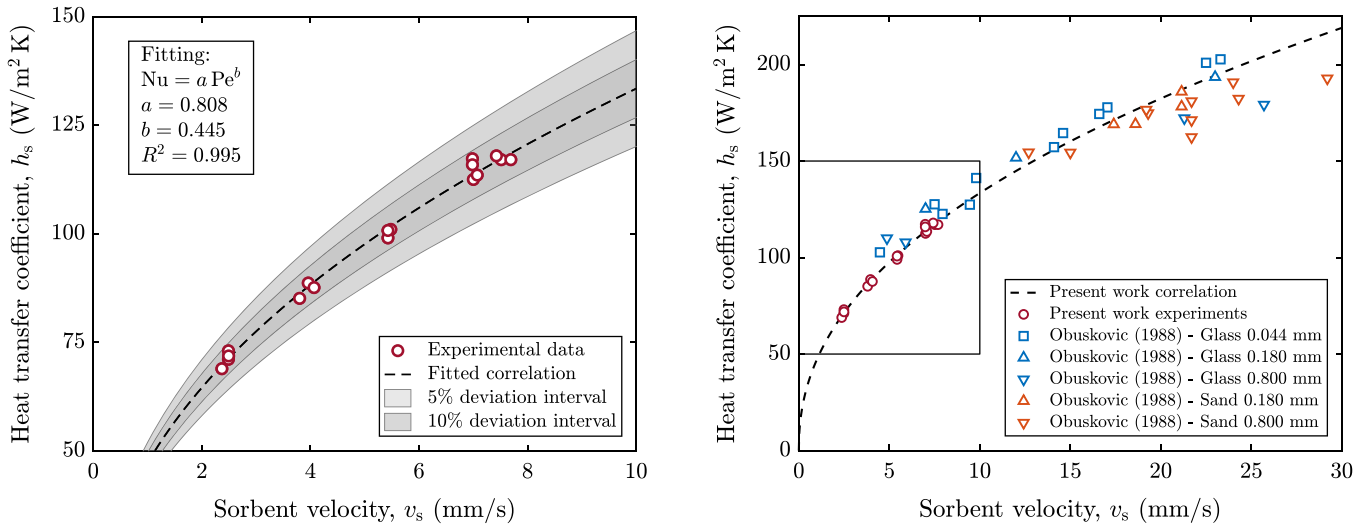


**Fig. 3.** Experimental heat transfer coefficients and fitted correlation (left). Comparison of the heat transfer coefficients measured in this work against the values reported by Obuskovic (1988) for a single tube immersed in a moving bed operated with glass and sand particles of different diameters (right).

**Table 4**
Flue gas specifications of the waste-to-energy CHP plant.

| Parameter | Value | Unit |
|---|---|---|
| Mass flow rate | 55.9 | kg/s |
| Temperature | 30 | °C |
| Pressure | 101.5 | kPa |
| Simplified composition: | | |
| molar fraction of $CO_2$ | 11 | % |
| molar fraction of $N_2$ | 89 | % |

$$P_i = \frac{q_i^*}{K_{H,i}} \exp\left(A_i q_i^* + B_i q_i^{*2}\right), \tag{12}$$

where subscript $i$ indicates the adsorbate ($CO_2$ or $N_2$), $P_i$ is the partial pressure, $q_i^*$ the amount adsorbed at equilibrium, and $K_{H,i}$ the Henry's law constant. The temperature dependence of the Virial coefficients $A_i$ and $B_i$ was expressed by

$$A_i = A_{0,i} + \frac{A_{1,i}}{T_s} \quad \text{and} \quad B_i = B_{0,i} + \frac{B_{1,i}}{T_s}, \tag{13}$$

while the dependence of the Henry's law constant with temperature was given by the Van't Hoff equation:

$$K_{H,i} = K_{H,i}^{\infty} \exp\left(\frac{-\Delta H_i}{R T_s}\right), \tag{14}$$

where $K_{H,i}^{\infty}$ is the adsorption constant at infinite temperature, $\Delta H_i$ the heat of adsorption at zero coverage, and $R$ the universal gas constant.

The values of the fitted Virial model parameters are summarized in Table 5, and they serve as basis for prediction of adsorption equilibrium in the MBTSA model, where the multi-component extension of the Virial model (Grande et al., 2008; Shen et al., 2010; Taqvi and LeVan, 1997) is implemented to account for competitive adsorption of the two gases (see Appendix A).

**Table 5**
Virial model parameters fitting $CO_2$ and $N_2$ adsorption isotherms on the activated carbon at temperatures between 30 and 150 °C and pressures up to 105 kPa.

| | $K_H^{\infty}$ mol / kg kPa | $-\Delta H$ kJ/mol | $A_0$ kg/mol | $A_1$ K kg/mol | $B_0$ kg$^2$/mol$^2$ | $B_1$ K kg$^2$/mol$^2$ |
|---|---|---|---|---|---|---|
| $CO_2$ | $2.6969 \cdot 10^{-7}$ | 30.006 | − 4.3235 | 1474.0 | 1.4239 | − 465.20 |
| $N_2$ | $5.5486 \cdot 10^{-7}$ | 21.934 | − 22.982 | 7121.1 | 51.644 | − 15756 |

The results of the $CO_2$ and $N_2$ isotherms measurements are shown in Fig. 4, together with the isotherms fitting, which was satisfactory for all the temperatures and pressures considered. As expected, the adsorption capacity of $CO_2$ is higher than that of $N_2$ in the whole temperature and pressure ranges examined. Nevertheless, the equilibrium selectivity expressed as

$$s_{CO_2/N_2} = \frac{q_{CO_2}/p_{CO_2}}{q_{N_2}/p_{N_2}} \tag{15}$$

and calculated at the feed gas conditions is just above 11. This value is significantly lower than that of other widely used $CO_2$ capture adsorbents, such as 13X and 5A zeolites, for which the selectivity can be as high as 96 and 90, respectively (Merel et al., 2008). Indeed, the $CO_2$ adsorption capacity at the feed gas conditions (11 kPa and 30 °C) is much lower for the activated carbon evaluated, being less than 0.4 mol/kg, compared to a value larger than 2 mol/kg for the zeolites (Cavenati et al., 2004; Mulloth and Finn, 1998). The $CO_2$ adsorption capacity of the material evaluated is also lower than that of other activated carbons reported in the literature at similar conditions (15 kPa and 30 °C): 0.6 mol/kg for a commercial BPL carbon, 0.9 mol/kg for a commercial Norit R2030CO2, and 1.0 mol/kg for a carbon honeycomb monolith (Plaza et al., 2017).

With regards to the heat of adsorption, the values obtained by fitting the $CO_2$ and $N_2$ isotherms are in agreement with literature data reported for other carbon adsorbents (Lopes et al., 2009; Mondino et al., 2017; Plaza et al., 2017).

### 3.3. MBTSA process configuration

The MBTSA process configuration considered in this work is illustrated in Fig. 5. The system comprises five main sections through which the adsorbent circulates, namely the adsorption, preheating, desorption, precooling and cooling sections. The separation of the $CO_2$ from the rest of the flue gas takes place within the adsorption section, where the gas flows upwards in a counter-current way with respect to the adsorbent that moves downwards. While the $CO_2$ is preferentially adsorbed onto the activated carbon, the non-adsorbing $N_2$ is vented to the atmosphere from the top outlet of the adsorption section. In order to ensure uniform distribution of the sorbent flow, the adsorption section is filled with structured packing consisting of corrugated and perforated metal plates,

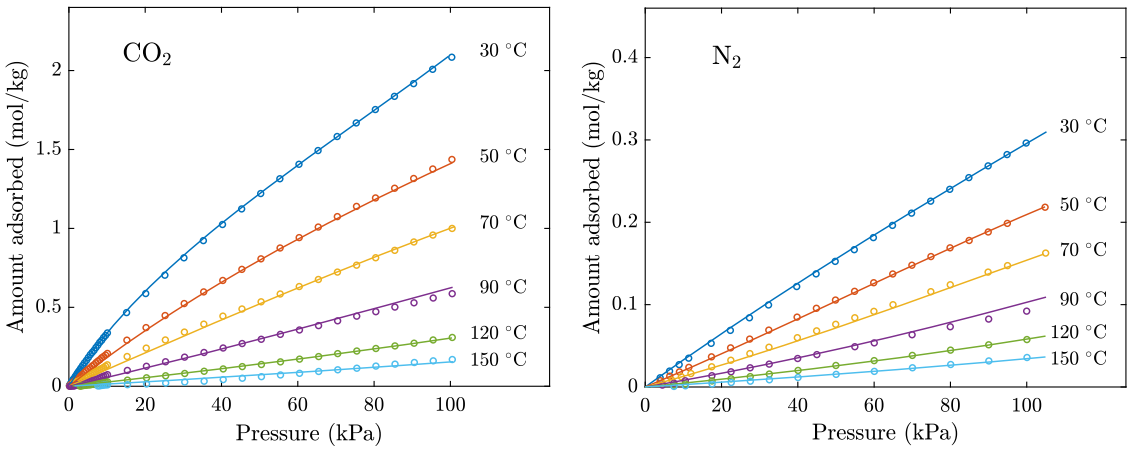


**Fig. 4.** $CO_2$ and $N_2$ adsorption isotherms on the activated carbon: measured data (dots) and model fitting (continuous lines).

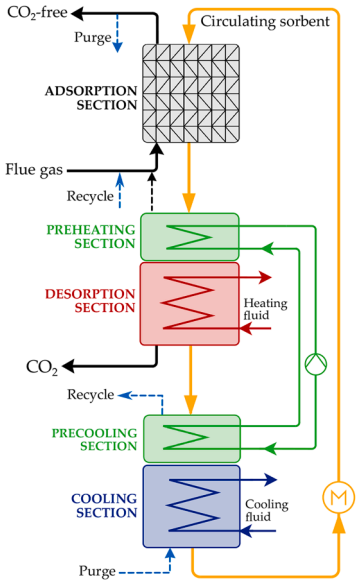


**Fig. 5.** Schematic diagram of the simulated MBTSA process.

similar to those used in absorption columns.

The adsorbent reaching the bottom outlet of the adsorbent section is loaded with $CO_2$ and needs to be regenerated. The thermal energy required for sorbent regeneration is provided within the preheating and desorption sections, both operated as indirect-contact heat exchangers. Pressurized water is used as heat transfer fluid. The preheating section is used first to heat the adsorbent to a certain extent by means of internally recovered heat, while the desorption section is used to provide additional heat to the sorbent until reaching the target desorption temperature. The desorbing $CO_2$ is collected in a $CO_2$-rich stream at the bottom end of the desorption section. Light vacuum (about 90 kPa) is applied to assist the desorption and direct the desorbing gas towards the extraction point.

The remaining sections, precooling and cooling, are used to bring the adsorbent back down to the adsorption temperature. If complete regeneration is not achieved within the desorption section, the remaining $CO_2$ is recovered by purging the adsorbent in the cooling and precooling sections with a small fraction of the $CO_2$-free product. Ultimately, the regenerated adsorbent is transported back to the top of the unit, closing the cycle.

### 3.4. Design of the MBTSA process

Based on the given flue gas specifications and adsorbent characteristics, the MBTSA process was designed to achieve a $CO_2$ purity of at least 95 % and a capture rate higher than 90 %, as typically required in CCS application (Joss et al., 2017; Nord and Bolland, 2020).

The design of the MBTSA process was accomplished using the one-dimensional model documented by the authors in previous publications (Mondino et al., 2017; 2019; 2020). The model is based on the mass, energy and momentum balances applied to the different MBTSA sections, and it was implemented in the gPROMS environment (gPROMS Model Builder Version 6.0, 2019). The dynamic simulations were performed until a steady state was reached, and all results presented here refer to the steady state solution. Compared to previous works, the model was extended to include the equations of the heating/cooling media of the heat exchangers and to accommodate the sorbent-side heat transfer coefficients determined experimentally. The complete set of model equations, together with the underlying assumptions, is reported in Appendix A.

Several design parameters including the system dimensions (height and diameter of each section) and operating conditions (amount of circulating sorbent, adsorption and desorption temperatures, and $CO_2$ extraction pressure) were adjusted until the target $CO_2$ purity and capture rate were achieved. The design parameters of the final configuration are listed in Table 6. A very large amount of sorbent (650 kg/s) relative to the flue gas (56 kg/s) was required because of the low $CO_2$ capacity of the adsorbent. The limited working capacity of the adsorbent was partially compensated by adopting a large temperature swing. In particular, the cooling and regeneration temperatures, i.e., the minimum and maximum temperatures experienced by the adsorbent, were 18 °C and 184 °C, respectively.

With regards to the system dimensions, the length and diameter of the adsorption section were selected as a trade-off to reduce the footprint of the column and limit the gas and sorbent velocities to avoid fluidization, guarantee a sufficient residence time, and limit the pressure drop. The cross section area of the other sections (preheating, desorption, precooling and cooling) was determined by scaling up the heat exchanger modules of the experimental apparatus to the actual sorbent flow rate, while maintaining the same tube shape and diameter (i.e., same heat transfer area per unit volume). The length was then adjusted so that the desired temperatures were reached by the end of the section.

### 3.5. Simulation results - concentration and temperature profiles

Figure 6 shows the computed concentration and temperature profiles along the five MBTSA sections, where the left and right limits of the plot correspond to the bottom of the cooling section and the top of the

**Table 6**
MBTSA design and process parameters.

| Operating conditions | | |
|---|---|---|
| Sorbent regeneration temperature | 184 | °C |
| Sorbent cooling temperature | 18 | °C |
| $CO_2$ extraction pressure | 90 | kPa |
| Inlet gas sup. velocity | 0.41 | m/s |
| Void fraction in adsorption section | 0.7 | - |
| Void fraction in other sections | 0.5 | - |
| System dimensions | | |
| Diameter in adsorption section | 12.8 | m |
| Diameter in other sections | 13.3 | m |
| Height of adsorption section | 0.9 | m |
| Height of preheating section | 0.4 | m |
| Height of desorption section | 0.8 | m |
| Height of precooling section | 0.4 | m |
| Height of cooling section | 0.6 | m |
| Total height | 3.1 | m |
| Sorbent inventory | | |
| Amount of circulating sorbent | 650 | kg/s |
| Sorbent mass flux in heat exchangers | 4.7 | $kg/m^2s$ |
| Sorbent residence time | 4.2 | min |
| Heating/cooling fluids (water) | | |
| Specific heat capacity | 4.2 | kJ/kg K |
| Density | 1000 | $kg/m^3$ |
| Flow rate in preheat./precool. sections | 160.6 | kg/s |
| Flow rate in desorption section | 267.6 | kg/s |
| Flow rate in cooling section | 267.6 | kg/s |
| Inlet temperature in desorption section | 187 | °C |
| Inlet temperature in cooling section | 10 | °C |

adsorption section, respectively. In agreement with this representation, the adsorbent flows from the right to the left in each section and the feed gas flows from the left to the right within the adsorption section.

As seen in the adsorbent loading profile within the adsorption section, a significant amount of nitrogen is also adsorbed along with the $CO_2$. This is in agreement with the adsorption equilibrium data and corresponding selectivity, which was estimated to be as low as 11. More specifically, at the bottom end of the adsorption section, i.e., at the gas feeding point, the fraction of nitrogen in the adsorbed phase is approximately 39% of the total, corresponding to a specific loading around 0.26 mol/kg, versus a $CO_2$ loading of 0.42 mol/kg. Furthermore, as seen in the temperature profile of the adsorption section, the effect of the heat of adsorption is modest and causes an increase in the adsorbent temperature of about 9 °C. As expected, in the adsorption section the maximum temperature is reached at the gas feeding point, where the adsorption driving force is the highest. The reason for the limited impact of this non-isothermal effect can be attributed to the high sorbent-to-gas ratio associated to the low adsorption capacity.

Most of the adsorbed nitrogen is released from the adsorbed phase as the temperature increases along the preheating section, i.e., moving from right to left along the plot, while the $CO_2$ loading remains approximately constant due to its stronger affinity on the adsorbent. The gas that is being desorbed within the preheating section is removed from the top and re-mixed with the feed gas (see Fig. 5). As the $N_2$ is removed, and the adsorbent temperature increases, the $CO_2$ fraction in the gas phase gradually increases towards the bottom end of the preheating section. The same trend continues in the desorption section, where the adsorbent temperature is further increased to the target

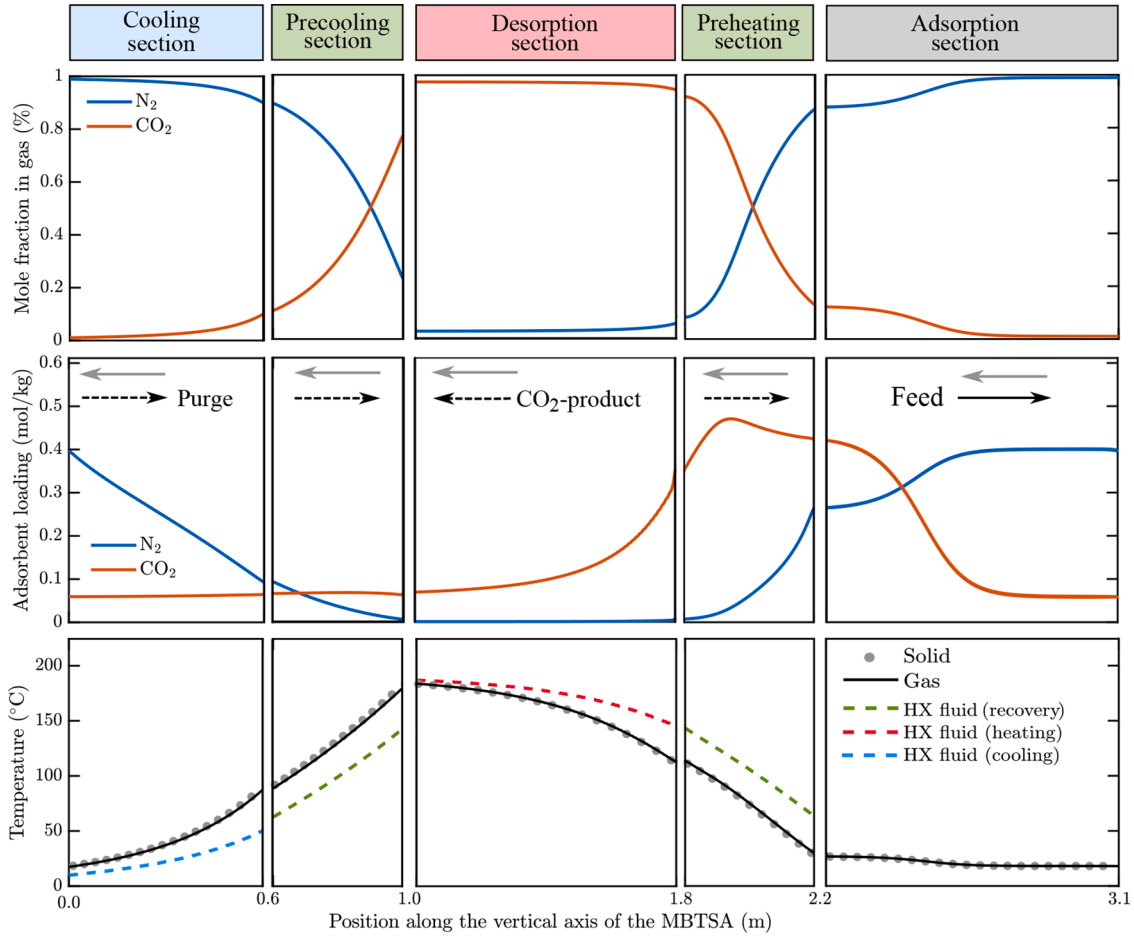


**Fig. 6.** Concentration and temperature profiles for each section of the MBTSA system. Position 0 m corresponds to bottom of the cooling section and position 3.1 m to the top of the adsorption section. The black and gray arrows represent the direction of the gas and sorbent flows, respectively.

regeneration temperature (184 °C) and $CO_2$ molar fraction in the gas phase reaches a maximum value of 97.2% at the bottom end of the section, i.e., the $CO_2$ extraction point.

As depicted in Fig. 6, the adsorbent still contains a certain amount of $CO_2$ (about 0.07 mol/kg) when entering the following section for pre-cooling. To further regenerate the adsorbent and recover this $CO_2$, a fraction of the $CO_2$-free product (approximately 15% of the total flow rate on a weight basis) was used to counter-currently purge the adsorbent within the cooling and precooling sections. The use of this purge gas is also important to avoid the formation of low pressure zones induced by the decrease in temperature, thus maintaining the pressure close to atmospheric.

In addition to the gas and sorbent temperature profiles, the bottom plot in Fig. 6 also shows the temperature of the heating and cooling fluids along the corresponding sections. In an attempt to maximize the internal heat recovery, the flow rate of the heat transfer media was tuned so that its heat capacity rate was as close as possible to that of the sorbent-gas side and the temperature difference along the heat exchanger was approximately constant.

### 3.6. Simulation results - overall system performance

The MBTSA process was evaluated in terms of several performance indicators, and the results are reported in Table 7. At steady state, the $CO_2$ purity corresponds to the molar fraction of $CO_2$ in the $CO_2$-rich product,

$$CO_2 \text{ purity} = \frac{\dot{n}_{CO_2,CO_2\text{-rich gas}}}{\dot{n}_{tot,CO_2\text{-rich gas}}} \cdot 100, \quad (16)$$

while the capture rate is obtained from an overall system mass balance as the ratio between the amount of $CO_2$ in the $CO_2$-rich product (i.e., moles of $CO_2$ captured per unit time) and the amount of $CO_2$ in the flue gas (i.e., amount of $CO_2$ fed to the system per unit time),

$$CO_2 \text{ capture rate} = \frac{\dot{n}_{CO_2,CO_2\text{-rich gas}}}{\dot{n}_{CO_2,\text{flue gas}}} \cdot 100. \quad (17)$$

The process productivity was calculated as the ratio between the mass flow rate of $CO_2$ in the $CO_2$-rich product and the total sorbent inventory,

$$\text{Productivity} = \frac{\dot{m}_{CO_2,CO_2\text{-rich gas}}}{\dot{m}_s \cdot t_{cycle}}. \quad (18)$$

The sorbent inventory is the amount of adsorbent needed to complete a full cycle and is calculated as the product of sorbent flow rate and the total cycle time (sum of residence time in each section). Lastly, the specific heat duty refers to the amount of thermal energy required to capture one kilogram of $CO_2$, and it was calculated by dividing the heat flow rate provided in the desorption section by the amount of $CO_2$ captured per unit time,

$$\text{Specific heat duty} = \frac{\dot{Q}_{\text{desorption section}}}{\dot{m}_{CO_2,CO_2-\text{rich gas}}}. \quad (19)$$

In spite of the low adsorbent selectivity, the designed MBTSA process was able to meet the desired target performance in terms of purity and capture rate, the obtained values being 97.2% and 90.8%, respectively. With regards to the energy use, the process requires 5.7 $MJ/kg_{CO_2}$, which is higher than other values reported in the literature for TSA capture processes achieving high $CO_2$ purity and recovery. For example, a value of 4.28 $MJ/kg_{CO_2}$ has been reported for a heat-integrated fixed-bed TSA system employing Zeolite 13X (Joss et al., 2017), while Merel et al. (2008) estimated 4.5 $MJ/kg_{CO_2}$ when using 5A zeolite. A slightly lower value (3.59 $MJ/kg_{CO_2}$) was reported by Plaza et al. (2017) referring to a TSA system based on structured carbon adsorbent and steam stripping. Nevertheless, the specific heat duty estimated in the present study is approximately three times higher than that of a similar case study previously documented by the authors (Mondino et al., 2019), where zeolite 13X was employed to capture $CO_2$ from a natural gas combined cycle (Mondino et al., 2019). The relatively higher energy duty can be explained by the much lower working capacity of the activated carbon (0.36 mol/kg) compared to that of the zeolite (2.8 mol/kg) which implies larger sorbent inventory and contributes to the parasitic duty associated to the sorbent heat capacity. In addition, to compensate for the low adsorption capacity towards $CO_2$, a high desorption temperature was adopted, which also led to an increase in the process energy requirement.

On the other hand, the simulated process seems to be very promising in terms of productivity, the obtained value being 181 $kg_{CO_2}/t_s h$. Such high process productivity can be attributed to the short cycle time (4.22 min) associated with the fast heating and cooling of the adsorbent. For comparison, Bonjour and co-workers calculated a productivity of 22.4 $kg_{ethane}/t_s h$ for a fixed bed TSA process with indirect heating for gaseous pollutant treatment (Bonjour et al., 2005). In the context of post-combustion $CO_2$ capture, Plaza et al. (2017) reported a productivity of 35–40 $kg_{CO_2}/t_s h$ when using carbon honeycomb monoliths in a fixed bed process with direct heating, while Joss et al. (2017) obtained a productivity between 30 and 60 $kg_{CO_2}/t_s h$ for an indirect heated TSA process using zeolite 13X achieving similar performance in terms of energetic consumption (about 4 $MJ/t_{CO_2}$), purity (above 95%), and capture rate (above 90%).

**Table 7**
Summary of simulations results.

| Main performance indicators | | |
|---|---|---|
| $CO_2$ purity | 97.2 | %vol |
| $CO_2$ capture rate | 90.8 | %vol |
| $CO_2$ captured | 8.26 | kg/s |
| Sorbent flow rate | 650 | kg/s |
| Process productivity | 181 | $kg_{CO_2}/t_s h$ |
| Specific heat duty | 5.7 | $MJ/kg_{CO_2}$ |
| Heat loads in MBTSA sections | | |
| Preheating (internal recovery) | 54.2 | MW |
| Desorption (external heating) | 47.0 | MW |
| Precooling (internal recovery) | 54.2 | MW |
| Cooling (external cooling) | 45.8 | MW |

## 4. Conclusions

The heat transfer coefficient on the sorbent side of a heat exchanger used for sorbent heating in an MBTSA system was determined in a lab scale apparatus. For this purpose, an activated carbon material shaped in spherical beads was circulated through a set of cross-flow shell-and-tube heat exchanger modules at different operating conditions (sorbent velocity and heating fluid temperature).

The analysis of the results revealed a direct dependence between the heat transfer coefficient and sorbent flow rate, while no dependence was observed on sorbent temperature. The trend of the experimental results suggested that operating the system at higher sorbent flow rates could lead to even higher heat transfer coefficients. In any case, the heat transfer coefficients obtained (69–117 $W/m^2$ K) are significantly higher than those typically encountered in fixed bed configurations (10–50 $W/m^2$ K). This confirmed that the moving bed configuration has the potential to address one of the main limitations of the fixed bed TSA process, namely, the low productivity due to the slow heating and cooling of the adsorbent.

The results of the experimental campaign were used to develop a correlation for the sorbent-side heat transfer coefficient in terms of the Nusselt and Péclet numbers. This correlation was incorporated into an MBTSA computational model, which was then used to design and analyze an MBTSA process for an industrial-scale waste-to-energy CHP

plant. The adsorbent material was the same commercial activated carbon used in the heat transfer experiments. Despite the low selectivity of the adsorbent, the proposed MBTSA process was able to achieve high $CO_2$ purity (97.2%) and capture rate (90.8%), at the expense of adopting a high regeneration temperature (187 °C) and solid-to-gas ratio (11.6 kg of adsorbent per kg of flue gas). These two factors led to a rather high heat consumption (5.7 MJ/$kg_{CO_2}$) compared with the values reported in literature for other adsorbents. Nevertheless, the designed MBTSA system was able to achieve high process productivity (181 $kg_{CO_2}/t_{ads}h$). This can be attributed to the fast temperature swings associated with the high sorbent-side heat transfer coefficient of the moving bed configuration. Overall, the simulation results indicate that the MBTSA technology is suited to capture $CO_2$ at high purity and recovery, while achieving higher process productivity than fixed bed TSA processes. However, the energy performance of the capture process was relatively poor, especially considering that 53.5% of the heat required to regenerate the adsorbent was provided by internal heat recovery. In this regard, it is believed that the thermal energy required may be significantly reduced by replacing the activated carbon material by other adsorbents having higher capacity and selectivity towards $CO_2$, such as zeolites or metal-organic frameworks.

## CRediT authorship contribution statement

**Giorgia Mondino:** Conceptualization, Methodology, Formal analysis, Writing – original draft. **Carlos A. Grande:** Conceptualization, Methodology, Writing – review & editing. **Richard Blom:** Funding acquisition, Project administration, Supervision. **Lars O. Nord:** Conceptualization, Methodology, Writing – review & editing, Supervision.

## Declaration of Competing Interest

The authors declare that they have no known competing financial interests or personal relationships that could have appeared to influence the work reported in this paper.

## Acknowledgments

We acknowledge the Research Council of Norway for its financial support through the EDemoTeC project (Grant no. 267873) within the CLIMIT program.

## Appendix A. MBTSA model equations

The MBTSA process is described by means of a one-dimensional mathematical model obtained by applying the mass, momentum and energy balances to the different sections (adsorption, preheating, desorption, precooling and cooling), each of which is connected to the adjacent ones through appropriate boundary conditions. Although the numerical value of certain design parameters (e.g., void fraction, section height, etc.) and operating conditions differ from section to section, the model equations and the underlying assumptions are the same for each section: negligible gradients in the radial direction, constant cross sectional area, constant sorbent velocity, uniform and constant void fraction, and ideal gas behavior in the bulk phase.

*Transport equations*

The gas phase concentration profiles along the section height are predicted by solving the mass balance in the gas phase for each species:

$$\varepsilon_c\frac{\partial C_i}{\partial t}+\frac{\partial(uC_i)}{\partial z}=\varepsilon_c\frac{\partial}{\partial z}\left(D_{z,i}C_T\frac{\partial Y_i}{\partial z}\right)-\frac{(1-\varepsilon_c-\xi)a'k_{f,i}}{\mathrm{Bi}_i/5+1}\left(C_i-C_{p,i}\right), \tag{A.1}$$

where the index $i$ corresponds to each component of the gas mixture, $t$ is the time; $z$ the position along the section height; $C_i$, $C_{p,i}$, and $Y_i$ the concentration in the bulk gas, the concentration in the macropores, and the molar fraction in the bulk gas, respectively; $\varepsilon_c$ the column void fraction; $\xi$ the volume fraction occupied by structured packing; $D_{z,i}$ the axial dispersion coefficient; $u$ the superficial gas velocity; $a'$ the adsorbent particle specific area; $k_{f,i}$ the film mass transfer coefficient; and $\mathrm{Bi}_i$ the Biot number. In addition, $C_T$ is the total concentration in the bulk gas, and it is computed with the ideal gas equation of state:

$$C_T=\sum_i C_i=\frac{P}{RT}, \tag{A.2}$$

where $P$ and $T$ are the pressure and temperature in the bulk gas, respectively, and $R$ is the universal gas constant.

Using the linear driving force (LDF) approximation to express the mass transfer rate from the bulk gas to the pores, and from the pores to the adsorbed phase, the mass balance in the macropores is given by:

$$\varepsilon_p\frac{\partial C_{p,i}}{\partial t}+v_s\frac{\partial C_{p,i}}{\partial z}=\varepsilon_p\frac{15D_{p,i}}{r_p^2}\frac{\mathrm{Bi}_i}{5+\mathrm{Bi}_i}\left(C_i-C_{p,i}\right)-\rho_p\frac{15D_{c,i}}{r_c^2}\left(q_i^*-q_i\right), \tag{A.3}$$

where $r_p$ is the particle radius, $D_{p,i}$ the macropore diffusivity, $\rho_p$ the particle density, $q_i$ the adsorbed concentration of component $i$, and $v_s$ the velocity of the adsorbent.

Similarly, the mass balance in the solid phase is given by:

$$\frac{\partial q_i}{\partial t}+v_s\frac{\partial q_i}{\partial z}=\frac{15D_{c,i}}{r_c^2}\left(q_i^*-q_i\right), \tag{A.4}$$

where $15D_{c,i}/r_c^2$ is treated as a single parameter representing the adsorption rate of component $i$, and $q_i^*$ is the adsorbed concentration of component $i$ in equilibrium with the corresponding local concentration in the macropore ($C_{p,i}$). The adsorption equilibrium is described with the multi-component extension of the Virial isotherm model (Grande et al., 2008; Taqvi and LeVan, 1997) that takes into account competitive adsorption of the

different species in the gas mixture:

$$P_i = \frac{q_i^*}{K_{\mathrm{H},i}} \exp\left[\sum_{j=1}^{N} A_{ij} q_j^* + \sum_{j=1}^{N}\sum_{k=1}^{N} B_{ijk} q_j^* q_k^*\right] \tag{A.5}$$

where the mixing Virial coefficients are calculated based on the fitting parameters from pure component measurements (Table 5) as:

$$A_{ij} = \frac{A_i + A_j}{2} \quad \text{and} \quad B_{ijk} = \frac{B_i + B_j + B_k}{3}. \tag{A.6}$$

The pressure gradient along the sections was computed using the Ergun equation (Ergun, 1952):

$$\frac{\partial P}{\partial z} = \frac{150\mu_{\mathrm{g}}(1-\varepsilon_{\mathrm{c}})^2}{\varepsilon_{\mathrm{c}}^3 d_{\mathrm{p}}^2} u + \frac{1.75(1-\varepsilon_{\mathrm{c}})\rho_{\mathrm{g}}}{\varepsilon_{\mathrm{c}}^3 d_{\mathrm{p}}} u|u|, \tag{A.7}$$

where $P$ is the total pressure in the bulk gas, $d_{\mathrm{p}}$ is the particle diameter, $\mu_{\mathrm{g}}$ is the gas viscosity, and $\rho_{\mathrm{g}}$ the gas density.

The gas and adsorbent temperatures ($T$ and $T_{\mathrm{s}}$) are computed from the energy balance in the gas phase and solid phases, respectively:

$$\varepsilon_{\mathrm{c}} C_{\mathrm{T}} \widehat{c}_v \frac{\partial T}{\partial t} + u C_{\mathrm{T}} \widehat{c}_p \frac{\partial T}{\partial z} = \frac{\partial}{\partial z}\left(\lambda_{\mathrm{g}} \frac{\partial T}{\partial z}\right) + \varepsilon_{\mathrm{c}} RT \sum_i \frac{\partial C_i}{\partial t} - (1-\varepsilon_{\mathrm{c}}-\xi) a' h_{\mathrm{gs}}(T - T_{\mathrm{s}}) - \alpha_{\mathrm{gt}} h_{\mathrm{gt}}(T - T_{\mathrm{t}}) \tag{A.8}$$

$$\begin{aligned}&\left[(1-\varepsilon_{\mathrm{c}}-\xi)\rho_{\mathrm{p}} c_{p,\mathrm{s}} + \xi \rho_{\mathrm{pk}} c_{p,\mathrm{pk}}\right]\left(\frac{\partial T_{\mathrm{s}}}{\partial t} + v_{\mathrm{s}} \frac{\partial T_{\mathrm{s}}}{\partial z}\right) = \xi \frac{\partial}{\partial z}\left(\lambda_{\mathrm{g_{pk}}} \frac{\partial T_{\mathrm{s}}}{\partial z}\right) + (1-\varepsilon_{\mathrm{c}}-\xi)\, a' h_{\mathrm{gs}}(T - T_{\mathrm{s}}) + \\ &(1-\varepsilon_{\mathrm{c}}-\xi)\rho_{\mathrm{p}} \sum_i \left( - \Delta H_i \left[\frac{\partial q_i}{\partial t} + v_{\mathrm{s}} \frac{\partial q_i}{\partial z}\right]\right) + (1-\varepsilon_{\mathrm{c}}-\xi)\varepsilon_{\mathrm{p}} RT_{\mathrm{s}} \sum_i \left[\frac{\partial C_{\mathrm{p},i}}{\partial t} + v_{\mathrm{s}} \frac{\partial C_{\mathrm{p},i}}{\partial z}\right]\end{aligned} \tag{A.9}$$

In the previous equations, $\Delta H_i$ represents the heat of adsorption of component $i$, $h_{\mathrm{gs}}$ the film heat transfer coefficient between the gas and the solid, $h_{\mathrm{gt}}$ the convective heat transfer coefficient between the gas and the tubes wall, $\alpha_{\mathrm{gt}}$ the heat transfer area per unit volume, $T_{\mathrm{s}}$ the temperature of the sorbent, $T_{\mathrm{t}}$ the temperature of the tubes wall, $\widehat{c}_v$ and $\widehat{c}_p$ the gas molar heat capacities at constant volume and constant pressure, respectively, $c_{p,\mathrm{s}}$ the specific heat capacity of the sorbent, $c_{p,\mathrm{pk}}$ the specific heat capacity of the packing, $\rho_{\mathrm{pk}}$ the density of the packing, $\lambda_{\mathrm{g}}$ the heat axial dispersion coefficient of the gas, and $\lambda_{\mathrm{pk}}$ the heat axial dispersion coefficient of the packing.

In addition, in the sections operated as indirect-contact heat exchanger, the temperature of the tubes wall ($T_{\mathrm{t}}$) and the temperature of the heating/cooling fluid ($T_{\mathrm{f}}$) are respectively given by:

$$\rho_{\mathrm{t}} c_{p,\mathrm{t}} \frac{\partial T_{\mathrm{t}}}{\partial t} = \alpha_{\mathrm{t,ext}} h_{\mathrm{gt}}(T - T_{\mathrm{t}}) - \alpha_{\mathrm{t,int}} h_{\mathrm{ft}}(T_{\mathrm{t}} - T_{\mathrm{f}}) \quad \text{and} \tag{A.10}$$

$$\rho_{\mathrm{f}} c_{p,\mathrm{f}} \frac{\partial T_{\mathrm{f}}}{\partial t} + u_{\mathrm{f}} \rho_{\mathrm{f}} c_{p,\mathrm{f}} \frac{L_z}{L_x} \frac{\partial T_{\mathrm{f}}}{\partial z} = -\alpha_{\mathrm{t,int}} h_{\mathrm{ft}}(T_{\mathrm{f}} - T_{\mathrm{t}}), \tag{A.11}$$

where the subscript t refers to the tubes wall, the subscript f refers to the heating/cooling fluid, $\alpha_{\mathrm{t,ext}}$ and $\alpha_{\mathrm{t,int}}$ are the external and internal heat transfer areas per unit of fluid volume, $h_{\mathrm{ft}}$ is the convective heat transfer coefficient between the heating/cooling fluid and the heat exchanger tubes, and the ratio $L_x/L_z$ is the distance travelled by the heating/cooling fluid per unit of height.

Equation (A.10) was derived assuming that the thermal conduction resistance of the walls is negligible, while taking into account the effect of the thermal capacity of the heat exchanger walls. On the other hand, Eq. (A.11) was derived considering a heat exchanger with a cross-flow shell-and-tube configuration, whereby the heating/cooling fluid flows within horizontal tubes. To this end, the energy balance was applied to a single tube along the direction of the fluid flow ($x$). The horizontal coordinate ($x$) was then converted to the axial coordinate along the section ($z$) by assuming a linear dependence of the tube length ($L_x$) with respect to the section length ($L_z$).

*Transport parameters*

The axial dispersion coefficients ($D_{z,i}$) controlling the diffusion term of the gas mass balances, Eq. (A.1), are obtained from the correlation proposed by Wakao and Funazkri (1978):

$$D_{z,i} = \frac{D_{\mathrm{m},i}}{\varepsilon_{\mathrm{c}}}(20 + 0.5\ \mathrm{Sc}_i\, \mathrm{Re}), \tag{A.12}$$

where the Schmidt and Reynolds numbers are defined as

$$\mathrm{Sc}_i = \frac{\mu_{\mathrm{g}}\rho_{\mathrm{g}}}{D_{\mathrm{m},i}} \quad \text{and} \quad \mathrm{Re} = \frac{\rho_{\mathrm{g}} u\, d_{\mathrm{p}}}{\mu_{\mathrm{g}}}, \tag{A.13}$$

with $\rho_{\mathrm{g}}$ and $\mu_{\mathrm{g}}$ being the gas density and viscosity, respectively, and $d_{\mathrm{p}}$ the particle diameter. The molecular diffusivities ($D_{\mathrm{m},i}$) are approximated with the Wilke correlation (Wilke, 1950):

$$D_{\mathrm{m},i} = \frac{1 - Y_i}{\sum_{j \neq i}^{n} \frac{Y_i}{D_{ij}}}. \tag{A.14}$$

where the binary diffusivity ($D_{ij}$) is given by Bird et al. (2002):

$$D_{ij} = \frac{0.01883\ T^{3/2}}{P\ \sigma_{ij}^2\ \Omega_{D_{ij}}} \sqrt{\frac{1}{M_{\mathrm{w},i}} + \frac{1}{M_{\mathrm{w},j}}}, \tag{A.15}$$

with $M_{\mathrm{w}}$ being the molecular weight of the gas species, $\sigma_{ij}$ the Lennard-Jones parameter, and $\Omega_{D_{ij}}$ the diffusion collision integral.

The source term of the gas mass balances, Eq. (A.1), involves the film mass transfer coefficients ($k_{\mathrm{f},i}$) and the Biot number of the adsorbent particles ($\mathrm{Bi}_i$). The former is estimated with the Sherwood number correlation proposed by Wakao and Funazkri (1978):

$$\mathrm{Sh}_i = \frac{k_{\mathrm{f},i} d_{\mathrm{p}}}{D_{\mathrm{m},i}} = 2.0 + 1.1 \mathrm{Re}^{0.6} \mathrm{Sc}_i^{1/3}, \tag{A.16}$$

while the Biot number is defined as

$$\mathrm{Bi}_i = \frac{r_{\mathrm{p}} k_{\mathrm{f},i}}{\varepsilon_{\mathrm{p}} D_{\mathrm{p},i}}, \tag{A.17}$$

where $r_{\mathrm{p}}$ is the particle radius, $\varepsilon_{\mathrm{p}}$ is the particle porosity and $D_{\mathrm{p},i}$ the macropore diffusivity. The macropore diffusivity is computed using the relation proposed by Yang (1987):

$$\frac{1}{D_{\mathrm{p},i}} = \tau_{\mathrm{p}} \left( \frac{1}{D_{\mathrm{Kn},i}} + \frac{1}{D_{\mathrm{m},i}}, \right) \tag{A.18}$$

where $\tau_{\mathrm{p}}$ is the particle tortuosity, and $D_{\mathrm{Kn}}$ is the Knudsen diffusivity, which is computed according to Ruthven (1984):

$$D_{\mathrm{Kn},i} = \frac{2}{3} r_{\mathrm{pore}} \sqrt{\frac{8}{\pi} \frac{RT}{M_{\mathrm{w},i}}}. \tag{A.19}$$

Moreover, the rate of adsorption of each component ($15 D_{\mathrm{c},i}/r_{\mathrm{c}}^2$), appearing in Eqs. (A.3) and (A.4), is assumed to have a dependency on temperature given by an Arrhenius equation:

$$\frac{15 D_{\mathrm{c},i}}{r_{\mathrm{c}}^2} = \frac{15 D_{\mathrm{c},i}^0}{r_c^2} \exp\left( \frac{-E_{\mathrm{a},i}}{RT} \right), \tag{A.20}$$

where the term $15 D_{\mathrm{c},i}^0 / r_{\mathrm{c}}^2$ represents the adsorption rate at infinite temperature and $E_{\mathrm{a},i}$ the activation energy of micropore/crystal diffusion.

In analogy with mass dispersion in the gas phase, the axial thermal dispersion coefficient ($\lambda_{\mathrm{g}}$) appearing in the gas energy balance, Eq. (A.8), is obtained from the empirical correlation proposed by Wakao et al. (1979):

$$\lambda_{\mathrm{g}} = k_{\mathrm{g}} (7 + 0.5\ \mathrm{Pr}\,\mathrm{Re}), \tag{A.21}$$

where the Prandtl number is defined as

$$\mathrm{Pr} = \frac{c_{p,\mathrm{g}} \mu_{\mathrm{g}}}{k_{\mathrm{g}}}, \tag{A.22}$$

with $k_{\mathrm{g}}$ being the gas thermal conductivity. In addition, the convective heat transfer coefficient between gas and solid ($h_{\mathrm{gs}}$) is computed with the Nusselt number correlation proposed by Wakao et al. (1979):

$$\mathrm{Nu} = \frac{h_{\mathrm{gs}} d_{\mathrm{p}}}{k_{\mathrm{g}}} = 2.0 + 1.1 \mathrm{Re}^{0.6} \mathrm{Pr}^{1/3}. \tag{A.23}$$

Lastly, the convective heat transfer coefficient on the sorbent-side of the heat exchanger ($h_{\mathrm{gt}} \equiv h_{\mathrm{s}}$) was computed with the correlation developed from the heat transfer measurements, see Eq. (11) in the main text.

## References


Akhtar, F., Andersson, L., Ogunwumi, S., Hedin, N., Bergström, L., 2014. Structuring adsorbents and catalysts by processing of porous powders. J. Eur. Ceram. Soc. 34 (7), 1643–1666.

Al-Ansary, H., El-Leathy, A., Al-Suhaibani, Z., Jeter, S., Sadowski, D., Alrished, A., Golob, M., 2012. Experimental study of a sand-air heat exchanger for use with a high-temperature solar gas turbine system. J. Sol. Energy Eng. 134 (4) https://doi.org/10.1115/1.4007585.

Baird, M.H.I., Rama Rao, N.V., Tackie, E., Vahed, A., 2008. Heat transfer to a moving packed bed of nickel pellets. Can. J. Chem. Eng. 86 (2), 142–150. https://doi.org/10.1002/cjce.20023.

Barrer, R.M., 1981. Sorption in porous crystals: equilibria and their interpretation. J. Chem. Technol. Biotechnol. 31 (1), 71–85.

Baumann, T., Zunft, S., 2015. Development and performance assessment of a moving bed heat exchanger for solar central receiver power plants. Energy Procedia 69, 748–757. https://doi.org/10.1016/j.egypro.2015.03.085.
Baumann, T., Zunft, S., Tamme, R., 2014. Moving bed heat exchangers for use with heat storage in concentrating solar plants: a multiphase model. Heat Transf. Eng. 35 (3), 224–231.
Berg, C. H., 1945. Adsorption process and apparatus.
Bird, R.B., Stewart, W.E., Lightfoot, E.N., 2002. Transport Phenomena, second ed. Wiley, New York.
Bonjour, J., Chalfen, J.-B., Meunier, F., 2002. Temperature swing adsorption process with indirect cooling and heating. Ind. Eng. Chem. Res. 41 (23), 5802–5811.
Bonjour, J., Clausse, M., Meunier, F., 2005. A TSA process with indirect heating and cooling: parametric analysis and scaling-up to practical sizes. Chem. Eng. Process. 44 (9), 969–977.
Bonjour, J., Rocha, L., Bejan, A., Meunier, F., 2004. Dendritic fins optimization for a coaxial two-stream heat exchanger. Int. J. Heat Mass Transf. 47 (1), 111–124.
Brunner, P.H., Rechberger, H., 2015. Waste to energy–key element for sustainable waste management. Waste Manage. 37, 3–12.
Bui, M., Adjiman, C.S., Bardow, A., Anthony, E.J., Boston, A., Brown, S., Fennell, P.S., Fuss, S., Galindo, A., Hackett, L.A., 2018. Carbon capture and storage (CCS): the way forward. Energy Environ. Sci. 11 (5), 1062–1176.
Campbell, C.S., 1990. Rapid granular flows. Annu. Rev. Fluid Mech. 22 (1), 57–90.
Cavenati, S., Grande, C.A., Rodrigues, A.E., 2004. Adsorption equilibrium of methane, carbon dioxide, and nitrogen on zeolite 13x at high pressures. J. Chem. Eng. Data 49 (4), 1095–1101.
Cengel, Y.A., Klein, S., Beckman, W., 1998. Heat Transfer: A Practical Approach, Vol. 141. WBC McGraw-Hill Boston.
Dai, Y.L., Liu, X.J., Xia, D., 2020. Flow characteristics of three typical granular materials in near 2D moving beds. Powder Technol. 373, 220–231. https://doi.org/10.1016/j.powtec.2020.06.057.
Ergun, S., 1952. Fluid flow through packed columns. Chem. Eng. Prog. 48, 89–94.
Farmahini, A.H., Krishnamurthy, S., Friedrich, D., Brandani, S., Sarkisov, L., 2021. Performance-based screening of porous materials for carbon capture. Chem. Rev. 121 (17), 10666–10741.
Farrance, I., Frenkel, R., 2012. Uncertainty of measurement: a review of the rules for calculating uncertainty components through functional relationships. Clin. Biochem. Rev. 33 (2), 49.
gPROMS Model Builder Version 6.0, 2019. Process System Enterprise (PSE). UK.
Grande, C.A., Lopes, F.V., Ribeiro, A.M., Loureiro, J.M., Rodrigues, A.E., 2008. Adsorption of off-gases from steam methane reforming ($H_2$, $CO_2$, $CH_4$, CO and $N_2$) on activated carbon. Sep. Sci. Technol. 43 (6), 1338–1364.
Haaf, M., Anantharaman, R., Roussanaly, S., Ströhle, J., Epple, B., 2020. $CO_2$ capture from waste-to-energy plants: techno-economic assessment of novel integration concepts of calcium looping technology. Resour. Conserv. Recycl. 162, 104973.
Hornbostel, M., 2016. Pilot-Scale Evaluation of an Advanced Carbon Sorbent-Based Process for Post-Combustion Carbon Capture. Report. SRI International, Menlo Park, CA (United States).
Hornbostel, M.D., Bao, J., Krishnan, G., Nagar, A., Jayaweera, I., Kobayashi, T., Sanjurjo, A., Sweeney, J., Carruthers, D., Petruska, M.A., 2013. Characteristics of an advanced carbon sorbent for $CO_2$ capture. Carbon 56, 77–85.
Hornbostel, M. D., Krishnan, G. N., Sanjurjo, A., 2015. Falling microbead counter-flow process for separating gas mixtures.
Isaza, P.A., Warnica, W.D., Bussmann, M., 2015. Co-current parallel-plate moving bed heat exchanger: an analytical solution. Int. J. Heat Mass Transf. 87, 616–624. https://doi.org/10.1016/j.ijheatmasstransfer.2015.02.079.
Joss, L., Gazzani, M., Mazzotti, M., 2017. Rational design of temperature swing adsorption cycles for post-combustion $CO_2$ capture. Chem. Eng. Sci. 158, 381–394. https://doi.org/10.1016/j.ces.2016.10.013.
Kaza, S., Yao, L., Bhada-Tata, P., Van Woerden, F., 2018. What a Waste 2.0: a Global Snapshot of Solid Waste Management to 2050. World Bank Publications.
Kearns, D. T., 2019. Waste-to-Energy with CCS: a pathway to carbon-negative power generation.
Kim, K., Park, Y.-K., Park, J., Jung, E., Seo, H., Kim, H., Lee, K.S., 2014. Performance comparison of moving and fluidized bed sorption systems for an energy-efficient solid sorbent-based carbon capture process. Energy Procedia 63, 1151–1161.
Kim, K., Son, Y., Lee, W.B., Lee, K.S., 2013. Moving bed adsorption process with internal heat integration for carbon dioxide capture. Int. J. Greenhouse Gas Control 17, 13–24.
Knaebel, K.S., 2005. Temperature Swing Adsorption System. US Patent 8353978B2.
Krishnamurthy, S., Haghpanah, R., Rajendran, A., Farooq, S., 2014. Simulation and optimization of a dual-adsorbent, two-bed vacuum swing adsorption process for $CO_2$ capture from wet flue gas. Ind. Eng. Chem. Res. 53 (37), 14462–14473.
LabVIEW, 2019. National Instruments. USA.
Lee, W., Youn, S., Park, S., 1998. Finite element analysis of the flow and heat transfer of solid particles in moving beds. Int. J. Energy Res. 22 (13), 1145–1155.
Lillia, S., Bonalumi, D., Grande, C., Manzolini, G., 2018. A comprehensive modeling of the hybrid temperature electric swing adsorption process for $CO_2$ capture. Int. J. Greenhouse Gas Control 74, 155–173.
Liu, Z., Grande, C.A., Li, P., Yu, J., Rodrigues, A.E., 2011. Multi-bed vacuum pressure swing adsorption for carbon dioxide capture from flue gas. Sep. Purif. Technol. 81 (3), 307–317.
Lopes, F.V., Grande, C.A., Ribeiro, A.M., Oliveira, E.L., Loureiro, J.M., Rodrigues, A.E., 2009. Enhancing capacity of activated carbons for hydrogen purification. Ind. Eng. Chem. Res. 48 (8), 3978–3990.
Marx, D., Joss, L., Hefti, M., Mazzotti, M., 2016. Temperature swing adsorption for postcombustion $CO_2$ capture: single-and multicolumn experiments and simulations. Ind. Eng. Chem. Res. 55 (5), 1401–1412.
Masala, A., Vitillo, J.G., Mondino, G., Martra, G., Blom, R., Grande, C.A., Bordiga, S., 2017. Conductive ZSM-5-based adsorbent for $CO_2$ capture: active phase vs monolith. Ind. Eng. Chem. Res. 56 (30), 8485–8498.
Merel, J., Clausse, M., Meunier, F., 2008. Experimental investigation on $CO_2$ post-combustion capture by indirect thermal swing adsorption using 13x and 5a zeolites. Ind. Eng. Chem. Res. 47 (1), 209–215.
Mickley, H.S., Fairbanks, D.F., 1955. Mechanism of heat transfer to fluidized beds. AlChE J. 1 (3), 374–384.
Mondino, G., Grande, C.A., Blom, R., 2017. Effect of gas recycling on the performance of a moving bed temperature-swing (MBTSA) process for $CO_2$ capture in a coal fired power plant context. Energies 10 (6), 745.
Mondino, G., Grande, C.A., Blom, R., Nord, L.O., 2019. Moving bed temperature swing adsorption for $CO_2$ capture from a natural gas combined cycle power plant. Int. J. Greenhouse Gas Control 85, 58–70. https://doi.org/10.1016/j.ijggc.2019.03.021.
Mondino, G., Spjelkavik, A.I., Didriksen, T., Krishnamurthy, S., Stensrød, R.E., Grande, C. A., Nord, L.O., Blom, R., 2020. Production of MOF adsorbent spheres and comparison of their performance with zeolite 13x in a moving-bed TSA process for postcombustion $CO_2$ capture. Ind. Eng. Chem. Res. 59 (15), 7198–7211. https://doi.org/10.1021/acs.iecr.9b06387.
Montañés, R.M., Flø, N.E., Nord, L.O., 2018. Experimental results of transient testing at the amine plant at technology centre mongstad: open-loop responses and performance of decentralized control structures for load changes. Int. J. Greenhouse Gas Control 73, 42–59.
Morales-Ospino, R., Santos, V.N., Lima Jr, A.R., Torres, A.E.B., Vilarrasa-García, E., Bastos-Neto, M., Cavalcante Jr, C.L., Azevedo, D.C., Marques, C.R., de Aquino, T.F., 2021. Parametric analysis of a moving bed temperature swing adsorption (MBTSA) process for postcombustion $CO_2$ capture. Ind. Eng. Chem. Res.
Mulloth, L.M., Finn, J.E., 1998. Carbon Dioxide Adsorption on a 5A Zeolite Designed for $CO_2$ Removal in Spacecraft Cabins. Report. National Aeronautics and Space Administration, Ames Research Center.
Niegsch, J., Köneke, D., Weinspach, P.-M., 1994. Heat transfer and flow of bulk solids in a moving bed. Chem. Eng. Process. 33 (2), 73–89.
Nord, L.O., Bolland, O., 2020. Carbon Dioxide Emission Management in Power Generation. John Wiley & Sons.
Obuskovic, N.S., 1988. Heat transfer between moving beds of solids and a vertical tube. Oregon State University. Ph.D. thesis.
Okumura, T., Ogino, T., Nishibe, S., Nonaka, Y., Shoji, T., Higashi, T., 2014. $CO_2$ capture test for a moving-bed system utilizi g low-temperature steam. Energy Procedia 63, 2249–2254. https://doi.org/10.1016/j.egypro.2014.11.243.
Okumura, T., Yoshizawa, K., Nishibe, S., Iwasaki, H., Kazari, M., Hori, T., 2017. Parametric testing of a pilot-scale design for a moving-bed $CO_2$ capture system using low-temperature steam. Energy Procedia 114, 2322–2329. https://doi.org/10.1016/j.egypro.2017.03.1369.
Plaza, M., Rubiera, F., 2019. Development of carbon-based vacuum, temperature and concentration swing adsorption post-combustion $CO_2$ capture processes. Chem. Eng. J. 375, 122002.
Plaza, M.G., González, A.S., Pevida, C., Rubiera, F., 2014. Influence of water vapor on $CO_2$ adsorption using a biomass-based carbon. Ind. Eng. Chem. Res. 53 (40), 15488–15499.
Plaza, M.G., Rubiera, F., Pevida, C., 2017. Evaluating the feasibility of a TSA process based on steam stripping in combination with structured carbon adsorbents to capture $CO_2$ from a coal power plant. Energy Fuels 31 (9), 9760–9775.
Qoaider, L., Thabit, Q., Kiwan, S., 2017. Performance assessment of a moving-bed heat exchanger with a sensible heat transfer medium for solar central receiver power plants. 2017 8th International Renewable Energy Congress (IREC). IEEE, pp. 1–5.
Rezaei, F., Webley, P., 2010. Structured adsorbents in gas separation processes. Sep. Purif. Technol. 70 (3), 243–256.
Ruthven, D.M., 1984. Principles of Adsorption and Adsorption Processes. John Wiley & Sons.
Rúa, J., Bui, M., Nord, L.O., Mac Dowell, N., 2020. Does CCS reduce power generation flexibility? A dynamic study of combined cycles with post-combustion $CO_2$ capture. Int. J. Greenhouse Gas Control 95, 102984.
Shen, C., Grande, C.A., Li, P., Yu, J., Rodrigues, A.E., 2010. Adsorption equilibria and kinetics of $CO_2$ and $N_2$ on activated carbon beads. Chem. Eng. J. 160 (2), 398–407.
Sjostrom, S., Krutka, H., 2010. Evaluation of solid sorbents as a retrofit technology for $CO_2$ capture. Fuel 89 (6), 1298–1306.
Son, Y., Kim, K., Lee, K.S., 2014. Feasibility study of a moving-bed adsorption process with heat integration for $CO_2$ capture through energy evaluation and optimization. Energy Fuels 28 (12), 7599–7608.
Takeuchi, H., 1996. Particles flow pattern and local heat transfer around tube in moving bed. AlChE J. 42 (6), 1621–1626.
Taqvi, S.M., LeVan, M.D., 1997. Virial description of two-component adsorption on homogeneous and heterogeneous surfaces. Ind. Eng. Chem. Res. 36 (6), 2197–2206.
Thermoflow Version 27, 2017. Termoflow Inc.
Tian, X., Yang, J., Guo, Z., Wang, Q., Sunden, B., 2020. Numerical study of heat transfer in gravity-driven particle flow around tubes with different shapes. Energies 13 (8). https://doi.org/10.3390/en13081961.
Turan, G., Zapantis, A., Kearns, D., Tamme, E., Staib, C., Zhang, T., Burrows, J., Gillespie, A., Havercroft, I., Rassool, D., Consoli, C., Liu, H., 2021. Global Status of CCS 2021. Report. Global CCS Institute, Melbourne, Australia.
Wakao, N., Funazkri, T., 1978. Effect of fluid dispersion coefficients on particle-to-fluid mass transfer coefficients in packed beds: correlation of sherwood numbers. Chem. Eng. Sci. 33 (10), 1375–1384.

Wakao, N., Kaguei, S., Funazkri, T., 1979. Effect of fluid dispersion coefficients on particle-to-fluid heat transfer coefficients in packed beds: correlation of Nusselt numbers. Chem. Eng. Sci. 34 (3), 325–336.
Wankat, P.C., 2006. Separation Process Engineering. Pearson Education.
Wilke, C.R., 1950. Diffusional properties of multicomponent gases. Chem. Eng. Prog. 46 (2), 95–104.
Yang, R.T., 1987. Gas Separation by Adsorption Processes, Vol. 1. World Scientific.
Zanco, S.E., Ambrosetti, M., Groppi, G., Tronconi, E., Mazzotti, M., 2021. Heat transfer intensification with packed open-cell foams in TSA processes for $CO_2$ capture. Chem. Eng. J. 131000.
Zanco, S.E., Joss, L., Hefti, M., Gazzani, M., Mazzotti, M., 2017. Addressing the criticalities for the deployment of adsorption-based $CO_2$ capture processes. Energy Procedia 114, 2497–2505.
Zanco, S.E., Mazzotti, M., Gazzani, M., Romano, M.C., Martínez, I., 2018. Modeling of circulating fluidized beds systems for post-combustion $CO_2$ capture via temperature swing adsorption. AlChE J. 64 (5), 1744–1759.